Combined techniques and relevant image processing for quantitative statistical characterization of inclusions in elastomers

Thomas Glanowski, Matthieu Le Saux, V. Le Saux, Bertrand Huneau, Clément Champy, Pierre Charrier, Yann Marco

Post-print of an article published in *Rubber Chemistry and Technology* (2023) 96 (1): 59–89;
doi: https://doi.org/10.5254/rct.22.22970

COMBINED TECHNIQUES AND RELEVANT IMAGE PROCESSING FOR QUANTITATIVE STATISTICAL CHARACTERIZATION OF INCLUSIONS IN ELASTOMERS

THOMAS GLANOWSKI[1, 2], MATTHIEU LE SAUX[1, *], VINCENT LE SAUX[1], BERTRAND HUNEAU[3], CLEMENT CHAMPY[2], PIERRE CHARRIER[2], YANN MARCO[1]

[1] *ENSTA BRETAGNE, UMR CNRS 6027, IRDL, F-29200 BREST, FRANCE*
[2] *VIBRACOUSTIC – CAE DURABILITY PREDICTION DEPARTMENT, 44474 CARQUEFOU, FRANCE*
[3] *NANTES UNIVERSITÉ, ECOLE CENTRALE NANTES, CNRS, GEM, UMR 6183, F-44000 NANTES, FRANCE*

ABSTRACT

The properties of elastomeric materials are strongly influenced by the inclusions resulting from the ingredients and the elaboration process. A methodology is proposed to differentiate the inclusions harmful for fatigue (larger than a few µm) in elastomers according to their chemical nature, and to characterize them quantitatively with sufficient statistics. Three techniques are used and compared: digital optical microscopy (OM), scanning electron microscopy (SEM) associated with energy dispersive X-ray spectroscopy, and X-ray micro-computed tomography (µ-CT). Six materials are used to challenge the methodology. In addition to the usual metal oxides and carbon black agglomerates, three atypical types of inclusions are highlighted, generating specific detection difficulties. A relevant image analysis procedure is developed to automatically detect the inclusions from the acquired images, more objectively and accurately than with the classical thresholding methods. The morphology and the spatial distribution of the different inclusions populations are then determined. µ-CT is the most comprehensive and accurate method for classification and statistical characterization of inclusions. Furthermore, relevant data on the size distribution of inclusions can be obtained using backscattered electrons (SEM-BSE) or digital OM. SEM-BSE provides more accurate results than digital OM.

INTRODUCTION

The performance of a rubber part is related to the quality of the dispersion of the ingredients in the compound. This dispersion depends on the ingredients used and on the elaboration process (mixing, injection and curing)[1]. Typical ingredients used for rubber parts include carbon black (CB) or silica fillers and ZnO. A good dispersion of the ingredients is important to obtain a homogeneous mixture, good mechanical performances and consistency of properties within a batch and between batches. In addition, the inclusions and the agglomerates play a key role in the mechanical properties of these materials. For example, fatigue damage generally initiates at CB agglomerates[2] or at silica agglomerates[3], or at metal oxides[2,4]. It is therefore important to be able to characterize the fillers dispersion and the inclusions in rubber compounds. Indeed, the knowledge of this dispersion in space and in size allows to check the quality of the mix, to optimize the process parameters, and to establish the link between the microstructure and the properties of interest.

Many techniques have been proposed for several decades in the literature to analyze the micro- or macro-dispersion of ingredients (essentially of CB) in rubber materials:

- Observation of a thin slice (a few microns to a few tens of microns in thickness) of material by transmitted light optical microscopy (OM)[5,6]: the method relies on the effect of local heterogeneities on the absorption of light; the darker and brighter areas observed correspond respectively to CB agglomerates and to agglomerates pulled off during the cutting; this method was adopted in the 1960s as a standard (ASTM D-2663 method B).

* Corresponding author. matthieu.le_saux@ensta-bretagne.fr

- Observation of the material surface after a manual cut or tear with a hand-held magnifying glass, a binocular or an optical microscope[6]: this method relies on the deviation of the breaking or cutting path by CB agglomerates, thus creating holes and "bumps"; it is based on the comparison of the rupture surface to a panel of images corresponding to different levels of dispersion. The smoother the surface, the better the dispersion. The visual inspection of a teared surface is used in the ASTM D-2663 (method A) standard. The principle of reference images was also used for surfaces obtained by cutting with a razor blade[7] observed with an oblique incident light. This process was then "automated"[8] and later became the current DisperGRADER™[9].
- Observation by dark field optical microscopy of the material surface cut with a razor blade[10,11]: the light paths of the illumination coming from the same side as the objective and those of observation are separated so that only the rays deviated by surface irregularities can reach the objective; the surface defects appear bright on a black background.
- Methods based on the optical properties of CB: due to the difference in light absorbance between the CB agglomerates and the elastomer matrix, the more the CB is dispersed, the darker the region[12,13]. This method allows to characterize the dispersion at the aggregate scale (*i.e.* for a size smaller than 1 µm).
- White light interferometry on the surface of a sample cut with a razor blade[14] (ASTM D2663 method D standard): this method allows to characterize the surface topography; holes and bumps are detected using image processing and height offset.
- Transmission electron microscopy (TEM): this technique uses an accelerated beam of electrons which is transmitted through the sample to form an image; CB appears black because of its higher density than the matrix. It has been used to analyze solutions obtained by dissolving the elastomer[15] or thin slice (~40 nm) of material[16]. This technique offers a very high resolution but the size of the area that can be analyzed is limited. The dispersion is therefore evaluated at the aggregate level.
- Scanning electron microscopy (SEM) in secondary electrons (SE) mode: the filler dispersion is measured on the surface of a cut sample, on a larger scale than with TEM[6]. The dispersion is therefore analyzed at the scale of agglomerates (size larger than a few µm). The degree of dispersion is usually estimated by visual inspection. If the SEM is equipped with an energy dispersive X-ray spectroscopy (EDS) system, the chemical composition of the poorly dispersed inclusions can also be determined.
- X-ray micro-computed tomography (µ-CT)[17,18,19,20]: the gray levels in the images obtained correspond to X-ray attenuation; the inclusions have a higher or lower X-ray attenuation coefficient so that they appear lighter or darker than the matrix respectively. 3D information about the morphology and the spatial distribution of the inclusions can be obtained after image processing. Relatively large volumes of material can be analyzed. Moreover, no particular sample preparation is required.
- Roughness measurement of a surface cut with a razor blade: it is assumed that the surface roughness is due to the fact that CB agglomerates deflect the cutting path. This roughness can be measured using a roughness tester[21] as described in the ASTM D-2663 (method C) standard, or an atomic force microscope (AFM)[22, 23]. With the first technique, it is the CB agglomerates that are analyzed; in the second case, it is the aggregates.
- Electrical resistivity[24,25,26]: the electrical conductivity of CB is much higher than that of rubber alone so that the resistivity increases with the degree of dispersion. The measurement is not very sensitive to large "isolated" agglomerates of CB so it can be considered that it focuses on the aggregates.

The objective of the present work is to establish a relevant methodology that meets the six following specifications:

- *Specification 1 – Size of inclusions*: the method must be able to characterize the inclusions larger than few µm in size, as they mostly determine the fatigue properties of rubber materials, especially for crack initiation[27,28] (smaller inclusions are not of interest here). The methods based on the optical properties of CB, TEM, AFM and electrical resistivity are not adapted because they do not allow to characterize the macro-dispersion at the scale of the agglomerates.
- *Specification 2 – Sensitivity and objectivity*: the detection of the inclusions must be as objective as possible in order to limit the influence of the operator on the results. For example, the method must not be sensitive to sample preparation, biased by artifacts, *e.g.*, due to blade marks resulting from the cut, or to user input for image analysis. The majority of the techniques presented above are based on surface topographic analysis. Detection of surface irregularities, assumed to be due to CB (which is a strong assumption), can be done optically (dark field microscopy, interferometric microscopy and DisperGRADER™) or mechanically (probe roughness meter). Image processing is usually required to analyze the results. The main difficulties are the non-planarity of the sample and the presence of cut marks that can be, wrongly, attributed to inclusions. Image processing is delicate because it can be highly dependent on the operator. The inclusions are generally not automatically detected from SEM images because of the complexity of the image. The inspection is then visual and therefore qualitative and influenced by the judgment and experience of the operator. The method based on µ-CT also uses image processing to detect inclusions. It is often simpler as there is no problem with cut marks and surface planarity. However, other types of artifacts can alter the detection of inclusions (*e.g.*, artifacts due to very high absorption inclusions[17]). In addition, image processing in tomography is generally based on a simple gray level thresholding method that is very dependent on the overall contrast of the images and on the user's choice.
- *Specification 3 – Nature of inclusions*: the inclusions must be differentiated according to their chemical nature insofar they do not all have the same influence. The techniques relying on topographic surface analysis (*e.g.*, DisperGRADER™, interferometric microscopy and dark field microscopy) allows characterizing inclusions that are stiffer than the matrix. It is important to note that these can remain coated with matrix after cutting, leading to an overestimation of the inclusion size. The bumps on the cut surface are generally supposed to be only due to CB. However, there can be several populations of inclusions more rigid than the matrix. Consequently, these techniques do not make it possible to distinguish the different types of inclusions. Using µ-CT, it is possible to differentiate inclusions if they have sufficiently different densities. In order to have more precise information on the chemical composition of the inclusions, SEM associated with EDS can be used. Nevertheless, the CB agglomerates remain difficult to distinguish from the matrix because of their close chemical nature.
- *Specification 4 – Quantitative description*: the morphology (*e.g.*, size and shape) and the spatial distribution of the inclusions must be described accurately and quantitatively, in 3D, as these features can influence the effects of the inclusions on the material properties. Topographic analysis methods do not allow to determine accurately the shape of the inclusions as many inclusions remain coated after cutting so that the measurement is not done directly on the inclusion itself. Using transmitted light microscopy, the shape of the inclusions can be determined in 2D. µ-CT is the only method that allows to observe the inclusions directly and, in addition, in 3D. It is

therefore possible to characterize their morphology, orientation and spatial distribution in 3D, not only in 2D as with the other techniques mentioned.

- *Specification 5 – Statistical description*: the results must be statistically representative of the material. The analyzed area must be as large as possible while keeping a good spatial resolution to allow the description of the inclusions. Ideally, it should be larger than the representative volume element, *i.e.*, the smallest volume containing all the information, from a statistical point of view, characterizing the morphology and the distribution of the heterogeneities in the material. µ-CT is the technique with the largest analysis area, with the additional advantage of obtaining 3D information. Thus, the information obtained by µ-CT can be considered as more representative from a statistical point of view. 2D measurements can nevertheless provide results with sufficient statistics but for this, it is necessary to make many observations until a significant number of inclusions is detected.
- *Specification 6 – Simplicity, robustness and efficiency*: the method should be robust and efficient, *i.e.*, relatively easy to implement so that it could be applied in an industrial context. All the techniques based on topography analysis simply require sample cut with a razor blade so that they can be easy and quick to implement. Nevertheless, cutting generates artifacts that complicate observation and image analysis. The preparation of very thin slices for transmitted light microscopy is very delicate, time-consuming and can also suffer from artifacts (*e.g.* thickness variations) that hinder the analysis. µ-CT is insensitive to cutting artifacts. Thus, sample preparation is simple and fast. However, µ-CT image acquisition can be long (several hours typically), expensive and requires an experienced operator. OM and SEM techniques are less expensive, faster and less complex to use although the analysis of the measurements still requires a certain expertise.

Table 1 summarizes this comparison of the different techniques in relation to the six specifications set.

In the light of this analysis, this paper focuses on three complementary techniques, which are now relatively accessible in laboratories: digital OM, SEM associated with EDS and µ-CT. These techniques offer spatial resolutions appropriate to the size of the inclusions of interest here (> 10 µm typically). The digital OM used allows to make observations almost identical to those of dark field microscopy as well as to characterize the surface topography as could be done using interferometric microscopy. This technique is investigated because sample preparation and data acquisition are simple and fast. Nevertheless, as discussed in more detail below, it is not able to differentiate the nature of inclusions. So, SEM is investigated to take advantage of the chemical information that can be obtained using EDS. µ-CT is also used because of the large amount of information (*e.g.* representativeness of the results and 3D morphology of the inclusions) that it can provide for certain types of inclusions.

A special effort is made to optimize the image processing in order to characterize the inclusions more objectively and exactly that with the usual methods[3,4,19]. Six materials with six types of inclusions with different features are used to challenge the methodology. The automatic detection of these inclusions is associated with different types of difficulties, depending on the inclusion features such as: small size, low contrast with the matrix, brighter than the matrix in some case and darker in other cases, inner cavity, elongated complex shape, artifacts (called "metal-induced" artifacts in the following) due to very high density inclusions, inclusions close to each other.

The materials and the experimental procedures used are first described. Then, the different types of inclusions observed in the characterized materials are presented. The next section describes the tool developed to detect, in an automatic way, the inclusions from the images. It also presents the information studied on the morphology and spatial distribution of

the detected inclusions. Then, a section presents the information obtained by applying the tool to the images from the different techniques (*i.e.*, digital OM, SEM and µ-CT). At last, the techniques used are compared against the six specifications defined above.

MATERIALS AND EXPERIMENTAL PROCEDURES

MATERIALS AND SPECIMENS

Six rubber materials with different populations of inclusions are investigated. Their chemical compositions are given in Table 2. They are all sulfur vulcanized and fully formulated according to an industrial process. For confidentiality reasons, all the details of their formulation are not explicitly given. Natural rubber (NR, standard Malaysian rubber 10) and/or Isoprene rubber (IR), reinforced with N339 CB or N990 CB are used. Materials with hollow glass beads (HGB) or solid glass beads (SGB) are also studied to check the consistency of the methods on well-calibrated inclusions. The beads are almost perfectly spherical objects of about 200 µm in diameter. Hourglass-shaped injected specimens, referred to as AE2 in the following, are used (Fig. 1). They have a minimum diameter of 9 mm and a notch radius of 2 mm. They are representative of the manufacturing process used for automotive anti-vibration parts.

DIGITAL OM

The observations by digital OM are made on freshly cut surfaces. Several cutting techniques have been tested. It is finally chosen to cut the undeformed sample made with a razor blade at room temperature. The razor blade is lubricated with soapy water and introduced perpendicular to the sample surface by applying a vertical pressure, following[7], *i.e.*, without back and forth movement so that the cut surface is minimally degraded.

The Keyence VHX-5000 digital optical microscope is used. The observation is done using coaxial light only (it was not possible to correctly describe the topography of both the smallest and the largest bumps). x500 magnification is used. This magnification allows a spatial resolution (pixel size) of 0.385 µm sufficiently small to detect clearly small inclusions (~10 µm) and an observation area large enough to be able to observe large inclusions (~100 µm). The 1600x1200 pixels^2 images are assembled so that images cover an area of up to 7.7x7.7 mm^2. Nevertheless, the larger the area of analysis, the higher the probability of having cut marks, which makes the analysis of the image more complex. The areas of observation are carefully chosen such as very few marks are noticeable.

SEM

SEM and EDS characterizations are performed on sample surfaces freshly cut using the same procedure as for OM observations. The SEM and EDS characterizations are performed using the JEOL JSM-6060LA and JEOL JSM-IT300 microscopes (tungsten filament gun). Both secondary electrons (SE) and backscattered electrons (BSE) modes are used, in order to obtain topographic contrast and chemical (atomic number) contrast, respectively. The observations are made at 10^{-3} Pa pressure. The samples are not metallized before observation, as the electric conductivity of samples is sufficiently high due to the presence of CB. The measurements are performed with an acceleration voltage of 15 kV. The chemical composition of the surface is determined using EDS. The acceleration voltage of 15 kV allows the analysis of the main

elements present in the studied materials, *i.e.*, carbon, oxygen, sulfur and zinc. Analysis of zinc is based on L-shell emission lines while K-lines are used for the other elements. The measurements are reproduced at different positions in the analyzed region, to ensure the relevancy of the results.

Areas of 0.64×0.49 mm^2 are observed with a spatial resolution of 0.5 µm (1280x960 $pixels^2$ images). It is not possible to observe large areas with a very fine resolution since automatic assembly of SEM images is complicated. The 0.5 µm resolution chosen allows to analyze the largest possible area and to detect inclusions with an equivalent diameter greater than 3 µm.

µ-CT

Some µ-CT measurements are performed in the gauge region of AE2 specimens. These specimens are stretched at a maximum principal strain of about 50% using Plexiglas™ pillars to ensure that they are held and thus avoid spurious movement during the acquisition. The volume analyzed is approximately a cylinder of 9 mm in diameter and 6 mm in height.

In order to perform µ-CT measurements with a better resolution, smaller bar samples are also used. They are extracted from AE2 specimens using a sharpened metal tube of 4 mm diameter. During the cutting process, the tube is rotated with a drill and lubricated with soapy water. The analyzed volume is approximately a cylinder of 3 mm in diameter and 2.9 mm in height.

The µ-CT scans are performed using the Zeiss/XRadia Micro XCT 400 micro-tomography system. The sample is rotated over 360° by an angle of 0.25° so that 1440 images are collected on the charge-coupled device detector. The parameters used for image acquisition are given in Table 3. Spatial resolutions (voxel size) of 8.3 and 1.7 µm are achieved for the AE2 specimens and the bar samples, respectively.

Table 4 summarizes the observed areas and the spatial resolutions of the images obtained using the three techniques investigated.

NATURE OF INCLUSIONS

As shown in TABLE 5, six different types of inclusions are identified in the six materials studied, by associating digital OM, SEM in BSE mode, EDS and µ-CT. In addition to glass beads and to the classical metal oxides and CB agglomerates, more atypical inclusions, called “geode-type”, type 1 and type 2 in the following, are observed. The strength of adhesion of the inclusion with the matrix was qualitatively assessed based on the ease of extracting the inclusion from the matrix. The elasticity and brittleness of the inclusion were qualitatively estimated by extracting the inclusion and crushing it. The stiffness of the inclusion was compared qualitatively to that of the matrix by observing the cut surfaces (if the inclusion generates a bump on the surface, it is considered stiffer than the matrix) or by micro-indentation measurements (results not presented in this paper).

The metal oxides are mainly zinc oxides. As they are the densest inclusions in the formulation, they are the brightest on µ-CT and SEM-BSE images (Fig. 2). According to the observations made, metal oxides have a weak adhesion with the matrix and show a rigid behavior. Moreover, the largest ones seem to be brittle.

Almost no CB agglomerates is observed directly on the cut surface, *i.e.*, without rubber covering it. However, inclusions extracted from the bumps observed after cutting are found to be rigid, brittle, granular and composed essentially of carbon (Fig. 3), which allows to assume

that they are CB agglomerates. The presence of CB agglomerates in all the mixtures studied is confirmed by µ-CT.

Inclusions consisting of a cavity surrounded by a spherical envelope are observed in the NR-N339 material (FIG. 4). They are called "geodes" because of their resemblance with mineralogical geodes. The cavity is lined with material denser than the matrix, with rod-type structure. It contains more oxygen, zinc and sulfur than the matrix as well as traces of phosphorus. The envelope of the geode is less dense than the matrix while being more rigid. It seems to be perfectly bounded to the matrix. It contains carbon and less sulfur and zinc than the matrix. A sample containing a geode was maintained for 4h at 100°C in an oven. This temperature is below the curing temperature. The envelope around the cavity seems to have reduced, while the cavity does not seem to be altered. Moreover, the bump generated by the geode on the surface has flattened. Thus, the geodes may consist of low molecular weight organic compounds extracted by the heat treatment, such as antioxidants. Nevertheless, the origin of the geodes could not be clearly identified.

Other inclusions, called type 1, are observed in the NR/IR-N339 material (FIG. 5). They have a rather elongated complex shape. They present a good adhesion with the matrix. They show certain elasticity while being stiffer than the matrix. They are denser than the matrix and contain about twice as much zinc oxide as the matrix. These type 1 inclusions are only observed in the NR/IR-N339 mixture.

So-called type 2 inclusions are present in NR/IR-N339 and IR-N339 mixtures (FIG. 6). Their spherical shape, elasticity and very good adhesion to the matrix seem to be close to those of geode-type inclusions, but they do not have a cavity. Type 2 inclusions are less dense than the matrix. They are composed of less sulfur and zinc than the surrounding matrix, like geode-type inclusions. A heat treatment of 4h at 100°C was applied to a sample containing type 2 inclusions. A reduction of the inclusion is observed, suggesting that this type of inclusion is made of low molecular weight elements such as antioxidants or elements from the IR gum (this type of inclusion is only observed in IR-based materials).

IMAGE ANALYSIS DEVELOPED TO CHARACTERIZE THE INCLUSIONS

IMAGE PROCESSING

The images obtained by digital OM, SEM-BSE or µ-CT are processed to separate the sample from the background in case of µ-CT images, and to identify and separate the inclusions from the rubber matrix (segmentation) for all types of images. A tool written using the Python programming language has been developed for image processing to be able to use, with full control, advanced processing and analysis methods adapted to the specific needs of the study. Indeed, the Python ecosystem offers a variety of image processing algorithms compatible with 2D and 3D images[29]. Several techniques have been tested to perform the image segmentation. Fig. 7 shows a block diagram of the image processing protocol finally retained, applied to the images from digital OM, SEM-BSE or µ-CT.

Before segmentation, the images are pre-treated to improve the contrast between the inclusions and the matrix, reduce the noise and thus facilitate subsequent segmentation (Fig. 8). First, the gray level histogram is stretched, by clipping given percentages of the darkest and the lightest pixels/voxels (*e.g.*, 10% for the darkest pixels/voxels and 0.5% for the lightest ones) to the gray levels corresponding to black and white, respectively. Then, the gray level histogram is rescaled to values between 0 and 1 for practical reasons. The contrast between the inclusions and the matrix on µ-CT images depends on the chemical composition of the inclusions. The

metal oxides can be clearly identified. However, the contrast between the CB agglomerates and the matrix is very small and only the biggest agglomerates can be clearly detected.

Then, a median filter is applied to the images to reduce the noise while preserving edges. The window size used for the median filter is 9x9 pixels^2 for digital OM images, 3x3 pixels^2 for SEM images and 3x3x3 voxels^3 for µ-CT images. Finally, in the case of µ-CT images, the sample is separated from the background by applying a simple threshold on the gray level values (Fig. 8 (c)). The threshold value is chosen halfway between the two distinct peaks corresponding to the sample and the surrounding void.

In the case of rubber materials, image segmentation is commonly performed using thresholding algorithms[3, 4, 19]. Threshold selection from the gray level histogram of the image can be manual or automatic[30]. These methods can be effective when the contrast between the objects to be segmented (the inclusions in the present case) and the matrix is sharp. However, in the present case, the inclusions, brighter than the matrix, are not associated with distinct peaks on the gray level histogram, as shown in Fig. 8. Consequently, the chosen threshold has a strong influence on the shape and size of the largest inclusions detected (Fig. 9). This point is usually not investigated in papers dealing with characterization of inclusions in rubber.

To make the segmentation more accurate, robust and objective, the random walk algorithm[31] is used. Image segmentation is treated as an optimization problem on a weighted graph, where each node represents a pixel (in 2D) or a voxel (in 3D). First, to initialize the algorithm (semi-automatic algorithm), seeds (labeled vertices) belonging clearly either to the inclusions or to the matrix are defined by applying thresholds on the gray level. As shown in Fig. 10, the threshold value used to define the seeds for the matrix is set to the gray level for which the curvature of the grayscale histogram of the whole image changes. More specifically, in the right hand part of the peak corresponding mainly to the matrix for inclusions brighter than the matrix, and in the left hand part of the peak for darker inclusions. The threshold value used to define the seeds for the inclusions is set more or less arbitrary since the grayscale histogram usually does not show clear peak for the inclusions (or a small one). To label the regions that remain undetermined after this step, the random walk algorithm then computes for each pixel/voxel the probability that a random “walker” leaving that pixel/voxel reaches the seeded pixels/voxels. The transition probability is inversely proportional to the contrast (difference between the intensities of grayscale) between the neighboring pixels so that the walker is not allowed to cross the “edges” where the gradient of gray level are high. As shown in Fig. 11, the threshold values used to determine the seeds have only very little effect on the segmentation. Nevertheless, in the particular case of µ-CT performed on bar samples, the segmentation algorithm can partly include the metal-induced artifacts observed around some metal oxides.

The size of the data obtained by µ-CT is large (several gigabytes). In addition, the random walk segmentation algorithm requires a lot of memory. The multiprocessor system used (8 processors with 24 CPU cores, 6 Tb RAM) was not sufficient to process the volume in one go. Therefore, a parallelization of the computations has been implemented for the segmentation step. The 3D matrix is divided into 54 sub-volumes with an overlap of 50%. It is divided into 9 blocks in the plane of the specimen section and 6 blocks on its height. The calculation of each block is performed on several processors.

As illustrated in Fig. 12, after segmentation, only inclusions larger than the window size used for the median filter are kept for analysis to avoid artifacts, *i.e.*, inclusions larger than 9x9 pixels^2 for digital OM images, 3x3 pixels^2 for SEM images and 3x3x3 voxels^3 for µ-CT images. Consequently, the inclusions analyzed have an equivalent diameter larger than 5 µm for digital OM images, 3 µm for SEM images and 6 µm for µ-CT images. These sizes are relevant to the study of the fatigue properties. In addition, incomplete inclusions at the edge of digital OM and SEM images are excluded. The application of the median filter allows to "remove" the blade

marks when they are thin on OM images. Most of the remaining blade marks are identified after segmentation by considering that they correspond to objects whose shape factor (ratio between the major axis and the minor axis lengths of the ellipse that has the same moment of inertia as the region) is greater than 3. They are then excluded from the analysis (Fig. 12). In the case of SEM-BSE images, blade marks are much less visible and they are automatically removed with the segmentation processing applied. In the case of µ-CT images obtained on bar samples, the sample outer periphery appears bright on a few voxels. To exclude this ring, the image of the specimen is eroded by a few voxels. To separate very close inclusions at the end of segmentation, an erosion operation is applied followed by a dilation, using the same structuring element for both operations (FIG. 13).

MICROSTRUCTURAL INDICATORS

Each region detected, assumed to be an inclusion, is labeled and its characteristics are then determined. The boundary of the regions is approximated with a set of triangles obtained using the marching cubes method[32] (Fig. 14). Indeed, estimation of the volume and surface area of the inclusions is more accurate with this triangular mesh than with the original square or cube representation[33]. For each region, the following indicators are determined:

- size: area or volume, equivalent diameter of the circle or the sphere with the same area or volume as the region;
- shape: circularity $4\pi A/P^2$ in case of 2D analysis with A and P the region area and perimeter, respectively, or sphericity $\pi^{1/3}(6V)^{2/3}/A$ in case of 3D analysis with V and A the region volume and surface area, respectively (measure of how much the shape deviates from perfect circle or sphere, for which it is equal to 1) and shape factor (ratio between the major axis and the minor axis lengths) of the ellipse or ellipsoid with the smallest area or volume that encompasses the region;
- orientation: angles between one global axis of the image and the major axis of the ellipse or ellipsoid that has the same second moment as the region;
- position: coordinates of the centroid of the region bounding box.
- Note that in the literature, the morphology of the inclusions is often described only in terms of equivalent diameter. The inclusions are located from their centroid and their spatial distribution is then analyzed using the spatial point process statistics[34], on the basis of:
- the shortest distance between the centroids of the regions;
- the Ripley's K-function[35] associated to the centroids of the regions, *i.e.*, the mean number of centroids within a given radius r from any other centroid: $K(r) = \lambda^{-1}N^{-1}\sum_i\sum_{j\neq i} I(d_{ij})w_{ij}^{-1}$, where λ is the density of events, N is the observed number of points, $I(d_{ij})$ is the indicator function equal to 1 if the distance d_{ij} between the ith and the jth points is less than or equal to r and to 0 otherwise, and w_{ij} provides the edge correction. The Ripley's K-function values obtained are compared to those expected for a homogeneous Poisson point process consisting in a completely random point pattern for which $K(r) = \pi r^2$ in 2D and $K(r) = \frac{4}{3}\pi r^3$ in 3D. For a given search distance, values of the K-function above, between or below the envelopes corresponding to a homogeneous Poisson point process indicate that the point pattern is clustered, random or regular, respectively.

APPLICATION TO THE DIFFERENT MATERIALS

The image processing and analysis protocol described above has been applied to digital OM, SEM and µ-CT images. This section presents the results obtained from each of the techniques. First, the indicators that allow to distinguish or not one type of inclusion from another are described. Then, examples of results obtained are presented. The comparative analysis of the different techniques is done in the following section.

APPLICATION TO DIGITAL OM IMAGES

Digital OM images allows to characterize the bumps visible on the surface but without distinction between the types of inclusions at the origin of these bumps.

Fig. 15 gives an example of digital OM image on the NR-N339 material with the segmentation results obtained using the developed image processing. The bumps visible on the cut surface are well detected in number and shape by image processing. 3237 bumps are counted. Fig. 16 (a, b) shows the associated distributions of bumps' equivalent diameter and circularity. The bumps detected have an equivalent diameter of about 10 µm on average. They have in majority a rather circular shape. The populations of inclusions are indistinguishable on OM images since they are embedded in matrix. Only the glass beads are distinguishable because either they leave a perfectly spherical hole or the gum does not remain bounded to their surface. The analysis of large bumps has shown that they can originate from several types of inclusions. Numerous small bumps, *i.e.*, a few micrometers in diameter, are observed. In the literature, it is commonly assumed that these are CB agglomerates. However, an EDS analysis (which somehow allows a depth of about 1 µm to be chemically analyzed) performed over the entire surface suggests that most of the small bumps result from zinc oxide inclusions. Moreover, by analyzing a surface such as the one shown in Fig. 15, it is possible to characterize a large number of small inclusions but only very few inclusions larger than 30 µm. The Ripley's K-function applied to the bumps detected on the same image is shown in Fig. 16 (d), along with the K-function expected for a homogeneous Poisson point process consisting in a completely random point pattern. The spatial distribution of the bumps follows a homogeneous Poisson point process. This shows that the ingredients are well distributed in the material without aggregation.

APPLICATION TO SEM-BSE IMAGES

SEM-SE images are relatively sensitive to charging effects and most inclusions are not highlighted very well. Attempts to process the SEM-SE images did not yield satisfactory results. Inclusions denser than the matrix are clearly visible on SEM-BSE images. Thus, only SEM-BSE images are analyzed by image processing to characterize the inclusion populations.

Detection and distinction of the different types of inclusions.–The metal oxides not coated with matrix after cutting (potentially due to poor adhesion with the matrix) appear white on SEM-BSE images. Those that are embedded in the matrix are associated with a gray level between that of the matrix and that of the very bright inclusions.

CB agglomerates are not visible due to a density too close to that of the matrix and/or to a layer of matrix covering the agglomerates that is too thick compared to the penetration depth of electrons. The cavity containing phosphorus of the geode-type inclusions appears very bright on SEM-BSE images (Fig. 17 (a)). The surrounding area shows a gray level very close to that of the matrix. It is nevertheless distinguishable from the matrix because it has a

"cauliflower" texture. The thickness of this rim is not the same for all the observed geodes and can sometimes be very thin or even unobservable. As for CB agglomerates, type 1 inclusions are almost not visible on SEM-BSE images because of their density close to that of the matrix. Type 2 inclusions show low contrast with the matrix. However, they can be differentiated from the matrix thanks to their texture, and from geodes because they do not present a cavity whose periphery appears very bright (Fig. 17 (b)). The glass beads appear lighter than the matrix on SEM-BSE images. They are distinguishable from other types of inclusions (metal oxides and geode cavity) because they are spherical and have a calibrated diameter of about 200 µm. Nevertheless, the two types of beads used (*i.e.*, solid and hollow) cannot be distinguished from each other.

Finally, the metal oxides, the geode cavity and the glass beads are detected automatically by processing of SEM-BSE images. The CB agglomerates, the area surrounding the cavity of geode-type inclusions, type 1 inclusions and type 2 inclusions cannot be detected automatically because of their low contrast with the matrix. The bright inclusions observed in Fig. 18 are metal oxides and the largest one is probably the periphery of the cavity of a geode. However, the automatic processing used does not allow to distinguish between these two types of inclusions.

Characteristics of the inclusions.–Fig. 18 shows an example of SEM-BSE image obtained on the NR-N339 material, segmented using the image processing previously described. 326 inclusions are detected. Some of their characteristics are given in Fig. 19. Their average equivalent diameter is about 4 µm. The detected inclusions are rather circular. The average shortest distance between the centroids of the inclusions with a size larger than 3.2 µm is about 20 µm. The inclusions' centroids follow a homogeneous Poisson point process, showing that they are randomly distributed.

APPLICATION TO µ-CT IMAGES

Detection and distinction of the different types of inclusions.–The type of sample and the resolution of the µ-CT are chosen according to the nature of the inclusions studied and according to the volume necessary for the results to be representative, depending on the size of the targeted inclusions. Thus, the µ-CT performed with a resolution of 1.7 µm on bar specimens are used to analyze geodes and CB agglomerates because the detection of these inclusions requires a very good resolution. The µ-CT carried out with a resolution of 8.3 µm on AE2 specimens are used to analyze the type 1 inclusions and the glass beads because their large size imposes to analyze a large volume. FIG. 20 shows examples of the different types of inclusions observed by µ-CT.

The inclusion populations show different features generating different types of difficulties for automatic detection from the images, which allows evaluating the capabilities and limitations of the method. Table 6 summaries the characteristics considered to detect and distinguish the different types of inclusions.

It is relatively easy to detect glass beads because of their spherical geometry, their size and their gray level (in the volume of SGB or in the periphery of HGB) clearly lighter than that of the matrix (FIG. 20 (a)). Bright inclusions with an equivalent diameter greater than 150 µm are assumed to be glass beads. Indeed, metal oxides are smaller, there is no type 1 inclusions in the materials containing glass beads and the potential geode-type inclusions cannot be observed due to the insufficient resolution of the concerned µ-CT. However, glass beads are numerous and therefore close to each other. The main difficulty is therefore to separate them

Most of the glass beads are well detected (FIG. 21 (a)). Nevertheless, two or three glass beads or a glass bead with metal oxides stuck to it are sometimes detected as a single entity (FIG. 21 (b)).

Metal oxides are the brightest regions on µ-CT images (FIG. 20 (b)). It is relatively easy to distinguish them from the matrix (the different types of metal oxides cannot be distinguished from each other). However, they can be small, some of them are surrounded by metal-induced artifacts and they are sometimes close to each other, which makes separation difficult. It is considered that metal oxides correspond to solid objects (*i.e.*, without cavity) and of smaller dimensions than type 1 inclusions and glass beads. In the case of materials without type 1 inclusions and glass beads, no size limit is set to identify metal oxides. Metal-induced artifacts observed around some metal oxides are partly detected by the segmentation algorithm (FIG. 22) used so that the size of metal oxides with pronounced metal-induced artifacts is slightly overestimated.

For CB agglomerates, the main difficulty is that it is difficult to distinguish them from the matrix. CB agglomerates cannot be identified on µ-CT images with a resolution of 8.3 µm. However, as shown in FIG. 3 (a) and FIG. 20 (c), CB agglomerates larger than about 40 µm can be distinguished from the matrix in µ-CT images with a resolution of 1.7 µm, by the absence of metal oxides at these locations and by a few dark voxels probably corresponding to porosities within the agglomerate. To our knowledge, Kallungal *et al.*[19] were the only ones to date that have reported in the literature results clearly showing CB agglomerates in elastomers in µ-CT performed using a non-synchrotron source. Because the gray level histogram of the CB and the matrix are similar, it was not possible to automatically detect CB agglomerates by image processing. The detection and analysis of CB agglomerates (larger than approximately 40 µm) are performed manually. Thus, only the number and size of these inclusions are analyzed.

The main complication for geode-type inclusions is related to their complex structure with a cavity whose border appears clearly lighter than the matrix surrounded by a zone only slightly darker than the matrix. Geodes cannot be clearly highlighted on 8.3 µm resolution µ-CT because the cavity and the area surrounding it cannot be distinguished so that only a bright area is observed. On 1.7 µm resolution µ-CT images, geodes are distinguishable from other types of inclusions due to their cavity border appearing bright and the area surrounding the cavity appearing slightly darker than the matrix (FIG. 4 (a) and FIG. 20 (d)). Only the cavity of the geodes is detected by automatic processing of 1.7 µm resolution µ-CT images. Indeed, the part slightly darker than the matrix surrounding the cavity is not systematically visible especially for the smallest geodes. Therefore, the size of the geodes is underestimated by a factor of 1.5 to 3.

Type 1 inclusions have the particularity of presenting a complex and elongated shape (FIG. 5 (a) and FIG. 20 (e)). They appear lighter than the matrix, like metal oxides. Type 1 inclusions are generally larger than metal oxides. However, in the case of large metal oxides (*i.e.*, larger than 100 µm), important metal-induced artifacts usually appear. Thus, it is considered that bright inclusions of more than 100 µm and not associated with metal-induced artifacts are type 1 inclusions.

Last, as shown in FIG. 6 (a) and FIG. 20 (f), unlike the other inclusion populations, type 2 inclusions appear darker than the matrix. Type 2 inclusions are detectable by image processing only from µ-CT performed on AE2 specimens made of NR/IR-N339. In the IR-N339 material, these inclusions are visible on 1.7 µm resolution µ-CT. On the other hand, in this material, they cannot be detected automatically by image processing for µ-CT with a resolution of 8.3 µm because the contrast with the matrix is very low. In the NR/IR-N339 material, these inclusions are visible in µ-CT with resolutions of 1.7 µm and 8.3 µm. Nevertheless, in the case of µ-CT with a resolution of 1.7 µm, the contrast of these inclusions with the matrix is also too low for them to be detected by image processing. Thus, only the 8.3

µm resolution µ-CT images obtained for the NR/IR-N339 material were processed automatically. Image processing leads to the detection of many small objects. Based on the observations made (section Nature of inclusions), only objects with an equivalent diameter larger than 60 µm or a sphericity index higher than 0.7 are supposed to be type 2 inclusions.

Characteristics of the inclusions.–Fig. 23 shows the 201109 metal oxides and the 165 geodes detected in a NR-N339 bar sample by processing 1.7 µm resolution µ-CT images. Some of their characteristics are illustrated in Fig. 24. Table 7 gives the characteristics of the inclusions detected in the six materials analyzed, *i.e.*, the minimum, mean and maximum values as well as the standard deviation (std) of the equivalent diameter, the sphericity and the distance to the nearest neighbor centroid of the inclusions, in addition to their number and their volume fraction.

Glass beads.–As shown in Table 7 (a), the volume fraction of glass beads is higher in the NR-N339&HGB material than in the NR-N339&SGB material, in accordance with the similar mass of glass beads incorporated. Due to the difficulty to separate some of the glass beads, the number of glass beads is underestimated in both materials, in particular in NR-N339&HBG. In both materials, the average equivalent diameter is about 210 µm, *i.e.*, close to the theoretical diameter of 200 µm. The results indicate sphericity indexes of glass beads of 0.82 in the NR-N339&HGB mixture and of 0.85 in the NR-N339&SGB material. The sphericity value depends on the spatial discretization of the inclusion. For a perfect sphere, this index is theoretically 0.925 for images with a spatial resolution of 8.3 µm. The slight difference between the average sphericity obtained and that of a perfect sphere is due to the poor detection of glass beads very close to each other. The distance from each glass bead to its nearest neighbor is on average 334 µm in NR-N339&HGB and 364 µm in NR-N339&SGB. This difference can be explained directly by the larger number of glass beads in NR-N339&HGB. This value is overestimated because a number of glass beads are detected as a single entity. The Ripley's K-function shows that the glass beads arrange themselves according to an aggregation process in both materials (Fig. 25).

Metal oxides.–The results in Table 7 (b) show that the average size of the detected metal oxides depends on the resolution of the µ-CT. In the different materials, the average diameter is estimated to be 45 µm from 8.3 µm resolution µ-CT and 13 µm from 1.7 µm resolution µ-CT. The volume fraction of metal oxides is lower according to 8.3 µm resolution µ-CT of AE2 specimens than according to 1.7 µm resolution µ-CT of bar samples. Indeed, in the latter, more metal oxides of small dimensions are detected. The size distributions obtained with the two scales of analysis are consistent (for inclusions larger than 30 µm). The number of inclusions per unit volume obtained on the AE2 specimens (resolution of 8.3 µm) is close to that obtained on the bar samples (resolution of 1.7 µm) for inclusions smaller than 40 µm but higher for inclusions larger than 40 µm. This is mainly due to strong metal-induced artifacts and to a bad detection of the inclusions very close to each other in the case of 8.3 µm resolution µ-CT (Fig. 22). The results show that the addition of glass beads, the type of CB or the gum used do not significantly influence the size distribution of metal oxides. According to the sphericity values, the metal oxides have a rather spherical shape independently of the scale of observation and the mixtures considered. The distribution of metal oxides follows a homogeneous Poisson point process for the six materials studied, as illustrated in Fig. 24 (d) for the NR-N339 material. The nearest neighbor distance is approximately 120 µm for metal oxides larger than 30 µm, and 32 µm for oxides larger than 6 µm. No influence of the gum type, CB type or glass bead addition is observed.

CB agglomerates.–Materials made of a single type of gum contain more large CB agglomerates in number and volume fraction (Table 7 (c)). Very few CB agglomerates are observed in the NR/IR-N339 mixture. Very large CB agglomerates can be observed in the IR-N339 material in larger volume fraction and smaller number than in NR-N339.

Geode-type inclusions.–The 165 geodes detected in a NR-N339 bar sample by processing 1.7 µm resolution µ-CT images are illustrated in Fig. 23. Some of their statistical characteristics are shown in Fig. 24. As indicated in Table 7 (d), the geode cavity has an equivalent diameter of 41 µm on average and of 76 µm at the maximum. It can be assumed that the maximum equivalent diameter of geodes may exceed 100 µm when considering the portion that encompasses the cavity. The geodes are more numerous and have a larger volume fraction than the CB agglomerates. As suggested by the mean sphericity index and its standard deviation, the cavity of the geodes is not spherical, with some variability in shape from one inclusion to another. The distance to their nearest neighbor is 301 µm on average, which is 3 times greater than for the metal oxides in the same specimen. Fig. 24 (d) shows the Ripley's K-function determined for a 1656x1656x1656 μm^3 cube taken in the analyzed volume. The K-function of the 38 analyzed geodes seems to be slightly below the theoretical curve for a homogeneous Poisson point process. This is due to the small number of geodes analyzed. Indeed, the K-function of the geodes is in the interval of the K-function following a Poisson process of intensity equal to $38/(1656 \times 1656 \times 1656)$. The spatial distribution of the geodes can thus be considered as approximately random.

Type 1 inclusions.–According to the µ-CT performed on the NR/IR-N339 AE2 specimen, type 1 inclusions are fewer in number and lower in volume fraction than the metal oxides, but larger in size (Table 7 (e) to be compared to Table 7 (b)). Their equivalent diameter is 129 µm on average and 288 µm at maximum. The sphericity index shows that type 1 inclusions are less spherical than metal oxides. Type 1 inclusions are ellipsoidal, with a shape factor of 2.1 on average. As shown in Fig. 26, about half of the inclusions have a shape factor greater than 2. Therefore, the equivalent diameter is not an appropriate indicator for these inclusions. The inclusions have a privileged orientation along the axis of the AE2 specimen. The more the inclusion is elongated, the closer its orientation is to the AE2 specimen axis. The preferential orientation of type 1 inclusions seems to be driven by the material flow during injection. The average distance between two type 1 inclusions is 661 µm, *i.e.*, about 3 times greater than for metal oxides in the same specimen. According to the Ripley's K-function, they are randomly distributed (homogeneous Poisson point process).

Type 2 inclusions.–The characteristics of the type 2 inclusions obtained are given in Table 7 (f). In the analyzed AE2 sample, type 2 inclusions are as numerous as type 1 inclusions. Nevertheless, their volume fraction is five times lower. Indeed, they are smaller (average equivalent diameter of about 90 µm). The average size obtained after image processing for the NR/IR-N339 AE2 specimen is close to the one obtained by manual analysis for the NR/IR-N339 and IR-N399 bar samples. The standard deviation on the equivalent diameter is two times smaller than that of type 1 inclusions. Thus, the size of type 2 inclusions appears to be homogeneous. The shape of these inclusions seems rather spherical and homogeneous. Type 2 inclusions are more widely spaced on average than type 1 inclusions and metal oxides. The spatial pattern of type 2 inclusions follows a homogeneous Poisson point process.

COMPARISON OF THE DIFFERENT TECHNIQUES

This section compares digital OM, SEM and µ-CT, associated with the developed image processing, according to the six specifications mentioned in the Introduction. As summary is made in TABLE 8, as done in TABLE 1 for the techniques reported in the literature.

The second specification (sensitivity and objectivity) is from our point of view reached for the three techniques thanks to the image analysis protocol developed. The simplicity, robustness and efficiency (sixth specification) of the three techniques have already been briefly discussed in the Introduction. In summary, µ-CT requires simpler sample preparation than digital OM and SEM. However, the technique is less accessible and acquisition can be longer and more expensive, which can complicate its implementation in an industrial environment. For the three techniques, robustness and efficiency are improved by the developed image processing. The following discussion focuses on the four other specifications. Finally, a short discussion is conducted on the comparison between 2D and 3D measurements.

SIZE OF INCLUSIONS (SPECIFICATION 1)

Fig. 27 (a) compares the size distribution of the inclusions analyzed by digital OM (Fig. 15, pixel size 0.385 µm) and SEM-BSE (Fig. 18, pixel size 0.5 µm) in the NR-N339 material. The size of the inclusions is larger according to optical OM observations than according to SEM-BSE observations. Indeed, the inclusions remain covered with matrix and it is the bumps that the inclusions generate on the cut surface that are measured on OM images and not the inclusions themselves. Thus, analysis based on digital OM tends to overestimate the size of the inclusions. To determine the exact size of the inclusion from OM observations, it would be necessary to know the thickness of the gum that coats the inclusion, the shape of the inclusion, its orientation and the position of the cutting plane in the height of the inclusion. The number of inclusions larger than 5 µm per unit area is 108 mm^{-2} for the SEM-BSE image in Fig. 18 and 830 mm^{-2} for the digital OM image in Fig. 15. To obtain the number of inclusions larger than 5 µm per unit area determined by digital OM, all the detected inclusions larger than 3.2 µm should be considered in the SEM image. This suggests that the analysis of digital OM images leads to an overestimation of about 2 µm of the equivalent diameter of the inclusions on average, due to a ~1 µm-thick matrix coating covering the small metal oxides. It is therefore considered that analysis based on SEM-BSE images is more accurate than that based on digital OM images. However, a bias may also exist in the case of SEM-BSE for the inclusions that are coated. Indeed, because of the limited emission depth of BSE, the probability of measuring the largest dimension of the inclusion is lower when it is covered, so that its size is underestimated.

NATURE OF INCLUSIONS (SPECIFICATION 3)

Table 9 summarizes the ability of the different techniques to differentiate inclusions by nature. The digital OM technique gives access to the population of inclusions that are more rigid than the matrix. However, it does not allow to distinguish the nature of the inclusions (except glass beads) since they remain coated by the matrix after cutting.

The SEM technique in the BSE mode allows the differentiation of inclusions composed of elements of high atomic number such as zinc, phosphorus and silicon. Thus, the geode cavity (containing phosphorus), metal oxides and glass beads (silica) can be distinguished from the matrix, the type 2 inclusions and the CB agglomerates. However, they cannot be differentiated from each other automatically. Type 2 inclusions can be observed but not be detected automatically by image processing. CB agglomerates and type 1 inclusions cannot be detected. To detect them, it could be considered that all inclusions not visible in BSE mode but generating

a visible bump in SE mode are CB agglomerates and/or type 1 inclusions. Nevertheless, this would not allow differentiating these two types of inclusions in materials where they coexist.

Using µ-CT, it is possible to observe all the types of inclusions found in the materials used in this study, *i.e.*, metal oxides, large CB agglomerates, geodes, and type 1 and type 2 inclusions and glass beads. All these types of inclusions can be detected automatically by image processing, expect CB agglomerates which must be detected manually. The different populations of inclusions can be differentiated from each other with certain assumptions about their morphologies. µ-CT is thus the best method for the classification of inclusions with respect to their nature (once the features of the different types of inclusions are known).

QUANTITATIVE AND STATISTICAL DESCRIPTION (SPECIFICATIONS 4 AND 5)

For the NR-N339 material, ten times fewer inclusions are detected from the SEM-BSE image shown in Fig. 18 than from the digital OM image shown in Fig. 15, in part because the observation area is 14 times smaller. It must be mentioned that when the analysis resolution for SEM-BSE is improved, the number of small bright inclusions (probably metal oxides) detected increases. The µ-CT illustrated in Fig. 23 (volume analyzed: cylinder of approximately 3 mm in diameter and 3 mm in height) allows to detect 62 times more inclusions than the digital OM image in Fig. 15 (surface analyzed: 7.7x7.7 mm^2).

The number of inclusions per unit volume detected by µ-CT in the NR-N339 material is shown in Fig. 27 (b) versus the inclusion size. Fewer inclusions per unit length than with OM and SEM are detected, due to the lower spatial resolution. A greater fraction of inclusions larger than 15 µm is observed compared with digital OM and SEM-BSE-based observations. On the one hand, µ-CT makes it possible to examine a volume and thus to obtain results supposed to be representative. On the other hand, in addition to the limited size of the analyzed surface, digital OM and SEM-BSE observations are performed on cross-sections that do not necessarily intersect the inclusions at their largest dimension. This leads to a tendency to underestimate the proportion of large inclusions and to overestimate the proportion of small inclusions. Stereological methods[36] could be used to refine the determination of the inclusion's size distribution from results of 2D observations.

The comparison of Fig. 16 (b) and Fig. 19 (b) shows that the inclusions detected from SEM-BSE images are slightly less circular than those detected by digital OM. Indeed, the bumps appearing in OM images tend to be rounded by the matrix covering the inclusions while SEM-BSE images are expected to better reflect the real shape of the inclusions, in 2D. µ-CT provides more direct information on the 3D morphology of the inclusions. For example, as shown in Fig. 24 (b), the metal oxides analyzed in the NR-N339 material have a rather spherical shape, while the cavity of the geodes is more tortuous.

The three techniques used, *i.e.*, digital OM (Fig. 16 (d)), SEM-BSE (Fig. 19 (d)) and µ-CT (Fig. 24 (d)), lead to the same conclusion about the type of spatial distribution of the inclusions detected, *i.e.*, a random distribution (homogeneous Poisson point process), except for the glass beads. The distances to the nearest neighbor determined from digital OM (Fig. 16 (c)) and SEM-BSE (Fig. 19 (c)) are very close. They are smaller than those evaluated by µ-CT (Fig. 24 (c)) in particular because the spatial resolutions of digital OM and SEM measurements are better, and therefore allow the identification of a larger number of small inclusions per unit area. µ-CT has nevertheless the advantage of characterizing the spatial distribution in 3D.

2D VERSUS 3D MEASUREMENTS

The comparison of surface techniques, *i.e.*, digital OM and SEM-BSE, and the volume µ-CT technique is not direct since the inclusions are not detected in the same way. Thus, in order to investigate the link between 3D and 2D measurements, the characteristics of the inclusions present on a randomly chosen slice (2D) of the µ-CT are compared to the results obtained on the whole volume, for the NR-N339 material. Only metal oxides and geodes are considered here and these two types of inclusions are not differentiated, since a surface measurement makes it difficult to do so. 771 inclusions are detected on the 2D slice, and 201274 in the whole volume. Fig. 28 (a) compares the distributions of the equivalent diameter of the inclusions obtained from the 2D and the 3D measurements. The results are almost identical. This suggests that the number of inclusions analyzed is sufficient to be representative of the entire volume. The rather spherical shape of the detected inclusions favors this equivalence. The 2D and 3D analyses agree to show that the spatial distribution of the inclusions follows a homogeneous Poisson point process. However, Fig. 28 (b) shows that the analysis of a single slice of the µ-CT leads to an overestimation of the average and maximum distances to the nearest neighbor by about a factor of two. A surface measurement can thus give a good estimate of the average size of the inclusions if they are rather spherical, randomly distributed and counted in sufficient number, but the evaluation of the distance to the nearest neighbor is biased.

CONCLUSIONS

Three techniques, now commonly accessible in laboratories, are thoroughly investigated to characterize the inclusions larger than a few µm in elastomers: digital OM, SEM in BSE mode and associated with EDS analysis, and µ-CT. Six materials, with different types of matrix (NR, IR and NR/IR) and of CB (N339 and N990) and with or without addition of glass beads, are used to challenge the methodology. By combining the three techniques, six different types of inclusions were identified. In addition to the glass beads, and to the metal oxides and the CB agglomerates classically observed in such materials, three types of atypical inclusions called geode-type, type 1, type 2 inclusions, were found in some of the formulations.

The different populations of inclusions have different features, generating several types of difficulties for automatic detection from digital OM, SEM-BSE or µ-CT images, *e.g.*, small size, low contrast with the matrix, inner cavity, elongated complex shape, metal-induced artifacts or inclusions close to each other. An efficient and robust image analysis procedure was implemented to automatically detect the inclusions from digital OM, SEM-BSE and µ-CT images, more objectively and accurately than with the more classical thresholding method. The size, the shape, the orientation and the spatial distribution of the different populations of inclusions were determined with good statistics for the six materials studied, from µ-CT analysis in particular. It was thus possible to study the influence of the addition of glass beads, the type of matrix and the type of CB on the populations of inclusions.

Inclusions that are stiffer than the matrix can be detected by digital OM but their nature cannot be identified. This technique does not only evaluate the macro-dispersion of CB agglomerates as sometimes considered in the literature but also that of inclusions of different natures. SEM-BSE allows to characterize the inclusions in a more precise way than the digital OM, and allows to differentiate certain types of inclusions. µ-CT makes it possible to observe all the types of inclusions, and to differentiate them. To our knowledge, this is one of the first times that CB agglomerates have been highlighted by µ-CT using a non-synchrotron source. The inclusions could be detected in an automatic way from µ-CT images, with the exception of CB agglomerates. The results obtained by µ-CT tend to be more statistically representative than those obtained with the 2D techniques because of the 3D nature of the observations, the greater number of inclusions detected and the larger size of the zone analyzed. Unlike digital OM and

SEM, µ-CT allows the measurement of many inclusions larger than 30 µm. The morphology of the inclusions and their spatial arrangement can be determined with more accuracy from µ-CT. Nevertheless, a relatively good estimate of the size of the inclusions can be obtained from digital OM and SEM-BSE measurements when the analyzed inclusions are in sufficient number, randomly distributed and have a rather spherical shape. However, it is more difficult to obtain reliable and statistically representative information on the spatial distribution of inclusions from surface measurement.

ACKNOWLEDGEMENTS

We thank the ANRT for financial support (CIFRE 2016/0048) and F. Bertrand from GeM for performing the µ-CT measurements.

REFERENCES

[1] G.R. Cotten, Mixing of carbon black with rubber I. Measurement of dispersion rate by changes in mixing torque, RUBBER CHEM. AND TECHNOL. **57**, 118 (1984).
[2] B. Huneau, I. Masquelier, Y. Marco, V. Le Saux, S. Noizet, C. Schiel, and P. Charrier, Fatigue Crack Initiation in a Carbon Black–Filled Natural Rubber, RUBBER CHEM. AND TECHNOL. **89**, 126 (2016).
[3] V. Le Saux, Y. Marco, S. Calloch, and P. Charrier, Evaluation of the Fatigue Defect Population in an Elastomer Using X-Ray Computed Micro-Tomography, *Polym. Eng. Sci.* **51**, 1253 (2011).
[4] K. Le Gorgu Jago, Fatigue life of rubber components: 3D damage evolution from X-ray computed microtomography, *Constitutive Model for Rubber V*, Paris (France), 173, 2007.
[5] C.H. Leigh-Dugmore, Measurement of Dispersion in Black-Loaded Rubber, RUBBER CHEM. AND TECHNOL. **29**, 1303 (1956).
[6] W.M. Hess, Characterization of dispersions, RUBBER CHEM. AND TECHNOL. **64**, 386 (1991).
[7] N.A. Stumpe and H.E. Railsback, *Rubber World* **151**, 41 (1964).
[8] S. Persson, Dispersion of Carbon Black, *Polym. Test.* **4**, 45 (1984).
[9] S. Otto, O. Randl, O. Goncalves, and B. Cantaloube, New Reference Value for the Description of Filler Dispersion with the Dispergrader 1000 NT, *Kautschuk Gummi Kunststoffe* **7**, 390 (2005).
[10] P.C. Ebell and D.A. Hemsley, A novel optical method for estimating the dispersion of carbon black in rubbers, RUBBER CHEM. AND TECHNOL. **54**, 698 (1981).
[11] A.Y. Coran and J.B. Donnet, The dispersion of carbon black in rubber Part I. Rapid method for assessing quality of dispersion, RUBBER CHEM. AND TECHNOL. **65**, 973 (1992).
[12] J. Jansen and G. Kraus, New Method for Estimating Dispersibility of Carbon Blacks in Rubber, RUBBER CHEM. AND TECHNOL. **53**, 48 (1980).
[13] M. Gerspacher, L. Nikiel, H.H. Yang, C.P. O'Farrell, Reflectometry - A New Method of Measuring Filler Dispersion, RUBBER CHEM. AND TECHNOL. **71**, 17 (1998).
[14] A.P. Smith, T.L. Aybar, R.W. Magee, and C.R. Herd, Carbon black dispersion measurement in rubber vulcanizates via interferometric microscopy, RUBBER CHEM. AND TECHNOL. **77**, 691 (2004).
[15] F.P. Ford and A.Y. Mottlau, Studies in the dispersion of SRF carbon black in butyl rubber, RUBBER CHEM. AND TECHNOL. **26**, 115 (1953).
[16] Jean, D. Jeulin, S. Forest, S. Cantournet, and F. N'Guyen, A multiscale microstructure model of carbon black distribution in rubber, *J. Microsc.* **241**, 243 (2011).

[17]K. Le Gorgu Jago, X-Ray Computed Microtomography of Rubber, RUBBER CHEM. AND TECHNOL. **85**, 387 (2012).
[18]T. Glanowski, B. Huneau, Y. Marco, V. Le Saux, C. Champy, and P. Charrier, Fatigue initiation mechanisms in elastomers: a microtomography-based analysis, *MATEC Web of Conferences* **165**, 08005 (2018).
[19]J. Kallungal, L. Chazeau, J-M. Chenal, J. Adrien, E. Maire, C. Barres, B. Cantaloube, and P. Heuillet, Methodology for 3D characterization of microstructural defects in filled polymer using X-ray Tomography, *Constitutive Models for Rubber XI*, Nantes (France), 77, 2019.
[20] D. Penumadu, J.-C. Chin, S. Young, F. Ignatz-Hoover, T. Floyd, P. Chapman, Sulfur dispersion quantitative analysis in elastomeric tire formulations by using high resolution X-ray computed tomography. RUBBER CHEM. AND TECHNOL. **1**, 626 (2021).
[21]P.C. Vegvari, W.M. Hess, and V.E. Chirico, Measurement of Carbon Black Dispersion in Rubber by Surface Analysis, RUBBER CHEM. AND TECHNOL. **51**, 817 (1978).
[22]C.C. Wang, S.H. Wu, J.B. Donnet, and T.K. Wang, Microdispersion of Carbon Blacks in Rubber, Part I: Some Quantitative Aspects by AFM Image Analysis, RUBBER CHEM. AND TECHNOL. **79**, 783 (2006).
[23]I.A. Morozov, B. Lauke, and G. Heinrich, Quantitative Microstructural Investigation of Carbon-Black-Filled Rubbers by AFM, RUBBER CHEM. AND TECHNOL. **85**, 244 (2012).
[24]A.R. Kemp and D.B. Hermann, Dielectric measurements in the study of carbon black and zinc oxide dispersion in rubber, RUBBER CHEM. AND TECHNOL. 12, **317** (1939).
[25]B.B. Boonstra, Resistivity of unvulcanized compounds of rubber and carbon black, RUBBER CHEM. AND TECHNOL. **50**, 194 (1977).
[26]H.H. Le, S. Ilish, B. Jakob, and H.J. Radusch, Online characterization of the effect of mixing parameters on carbon black dispersion in rubber compounds using electrical conductivity, RUBBER CHEM. AND TECHNOL. **77**, 147 (2004).
[27]I. Masquelier, Influence de la formulation sur les propriétés en fatigue d'élastomères industriels, PhD thesis, Université de Bretagne Occidentale (France), 2014 (in french).
[28]J. Kim and H. Jeong, A study on the material properties and fatigue life of natural rubber with different carbon blacks, *Int. J. Fatigue* **27**, 263 (2005).
[29]E. Gouillart, J. Nunez-Iglesias, and S. Van Der Walt, Analyzing microtomography data with Python and the scikit - image library, *Adv. Struct. Chem. Imaging* **2** (2016).
[30]N. Otsu, A Threshold Selection Method from Gray-Level Histograms, *IEEE Transaction on System, Man, and Cybernetics SMC-9* **62** (1979).
[31]L. Grady, Random Walks for Image Segmentation, *IEEE Transactions of Pattern Analysis and Machine Intelligence* **28**, 1768 (2006).
[32]T. Lewiner, H. Lopes, A.W. Vieira, and G. Tavares, Efficient implementation of Marching Cubes' cases with topological guarantees, *Journal of Graphics Tools* **8**, 1 (2003).
[33]Nyström, J.K. Udupa, G.J. Grevera, and B.E. Hirsch, Area of and volume enclosed by digital and triangulated surfaces, *Proceeding SPIE **4681***, 669 (2002).
[34]P.J. Diggle, Spatio-temporal Point Processes: Methods and Applications, Johns Hopkins University, Dept. of Biostatistics Working Papers, Working Paper 78, 2006.
[35]B.D. Ripley, Modelling Spatial Patterns, *Journal of the Royal Statistical Society, Series B* **39**, 172 (1977).
[36]D.L. Sahagian, and A. Proussevitch, 3D particle size distributions from 2D observations: stereology for natural applications, *J. Volcanol. Geotherm. Res.* **84**, 173 (1998).

LIST OF FIGURES

FIG. 26. — Histogram of the shape factor of type 1 inclusions detected on a 8.3 µm resolution µ-CT obtained for the NR/IR-N339 material (AE specimen).
FIG. 27. — (a) Number of inclusions per unit area detected by digital OM and SEM-BSE and (b) number of inclusions per unit volume detected by µ-CT, versus the inclusion's equivalent diameter, for the NR-N339 material.
FIG. 28. — Comparison of the normalized histograms of (a) the equivalent diameter and (b) the shortest distance between the centroids of the inclusions (metal oxides and geodes) detected on a slice of the µ-CT (771 inclusions) and on the whole volume (201274 inclusions), for the NR-N339 material.

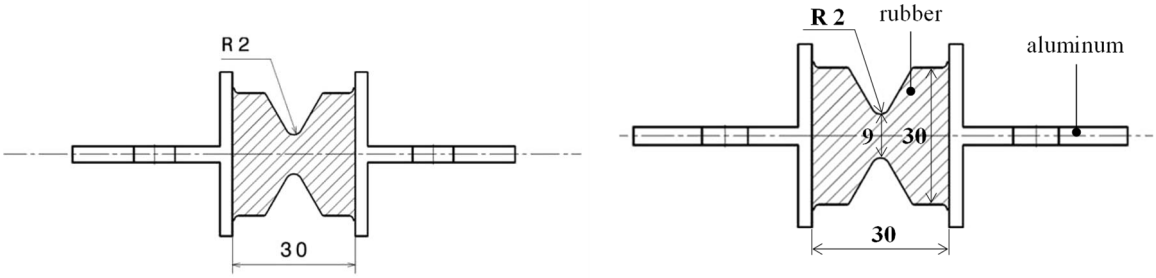

FIG. 1. — Hourglass-shaped specimen (AE2) used (dimensions in mm).

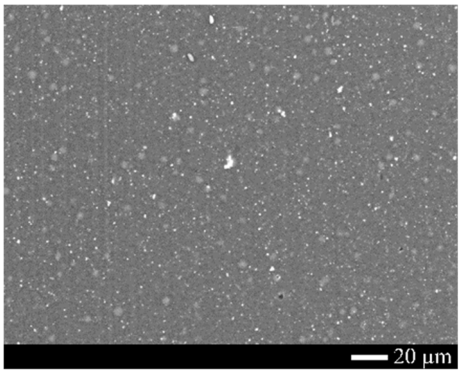

FIG. 2. — Metal oxides observed by SEM-BSE.

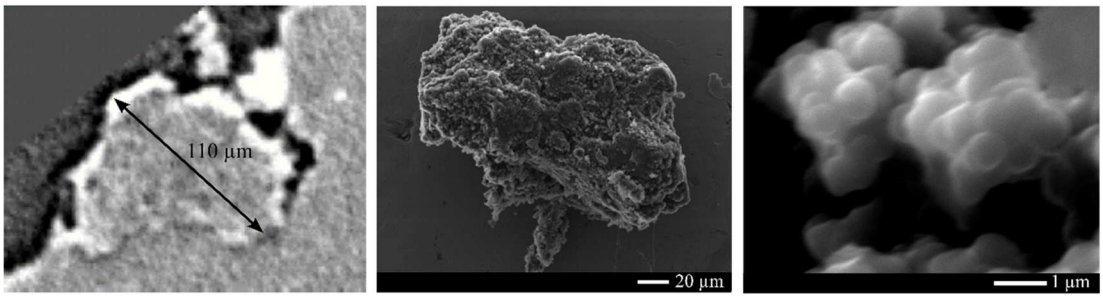

(a) (b) (c)

FIG. 3. — CB agglomerate (a) at the surface of a sample observed by µ-CT, and (b, c) extracted from the sample observed by SEM-SE at different magnifications.

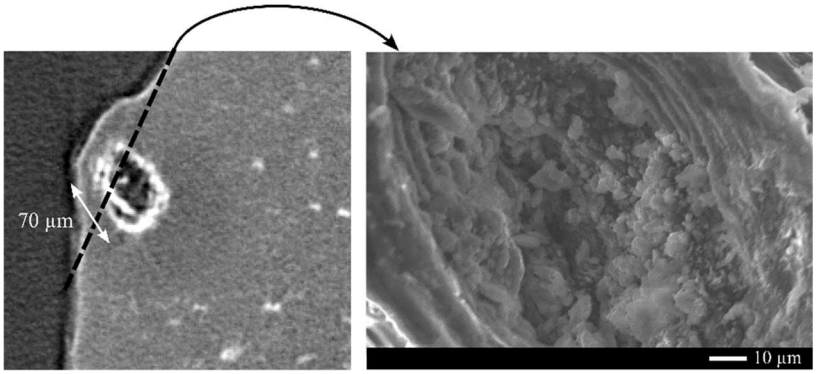

FIG. 4. — Geode-type inclusion observed (a) by µ-CT at the surface of a sample and (b) by SEM-SE after surface erosion.

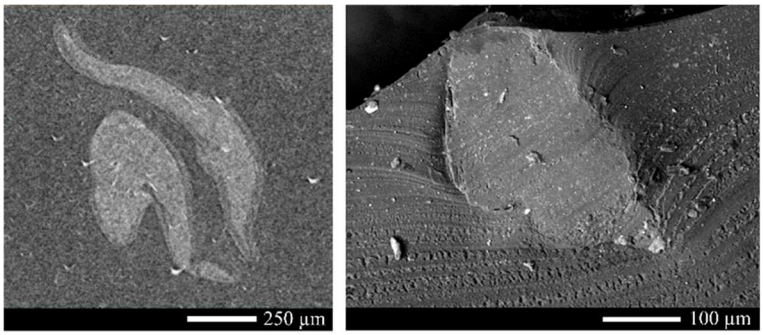

FIG. 5. — Type 1 inclusions observed (a) by µ-CT (0.54 µm resolution) and (b) by SEM-SE after being cut.

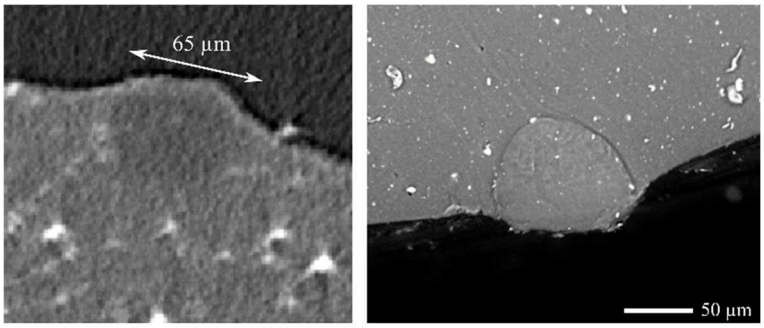

(a) (b)

FIG. 6. — Type 2 inclusion observed (a) by µ-CT (voxel size: 1.7 µm) and (b) by SEM-SE after being cut.

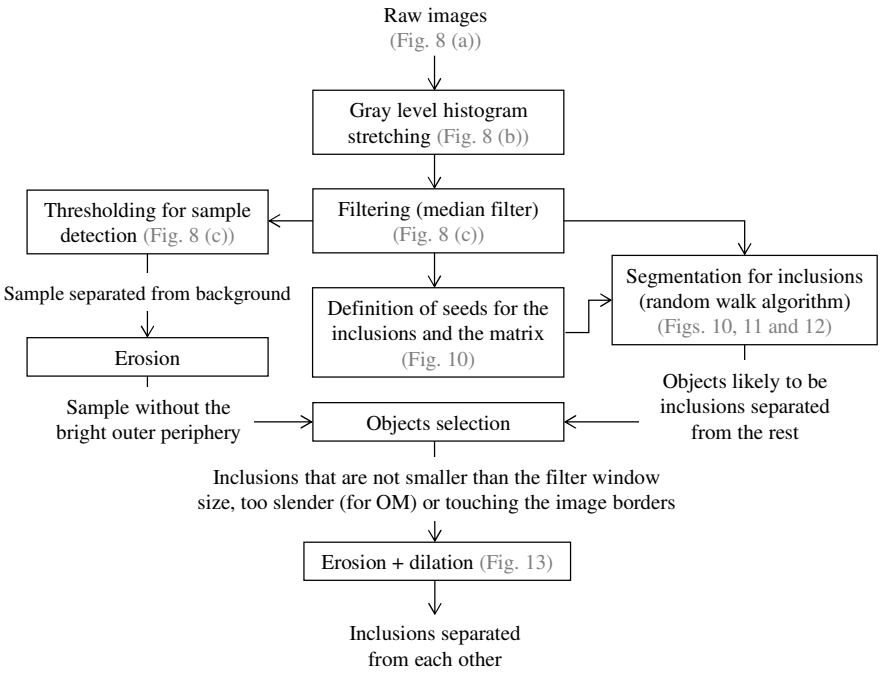

FIG. 7. — Block diagram showing the main steps of the image processing.

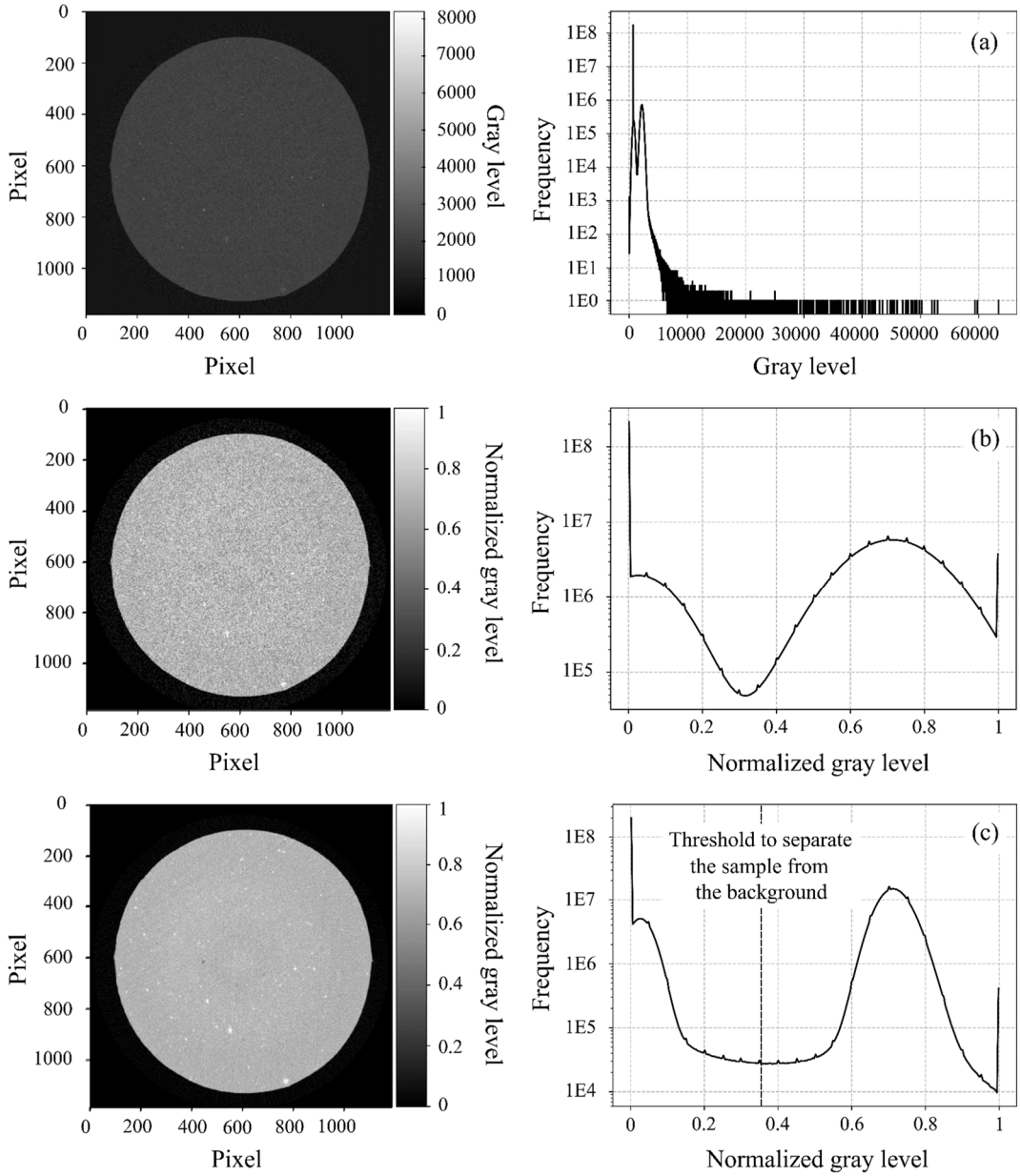

FIG. 8. — Image preprocessing on a µ-CT image (associated gray level histogram shown on the right): (a) initial image, (b) image after gray level histogram stretching, (c) image after application of a 3x3x3 voxels^3 median filter.

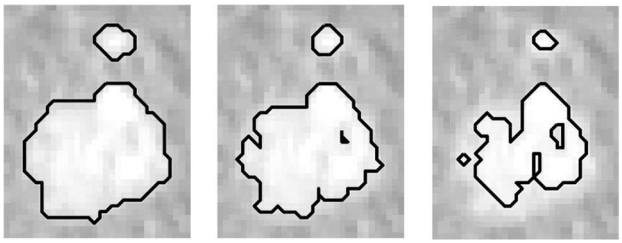

FIG. 9. — Segmentation of an inclusion on a μ-CT image using a thresholding method: sensitivity to the threshold value (for gray level histogram close to the one shown in Fig. 8(c)).

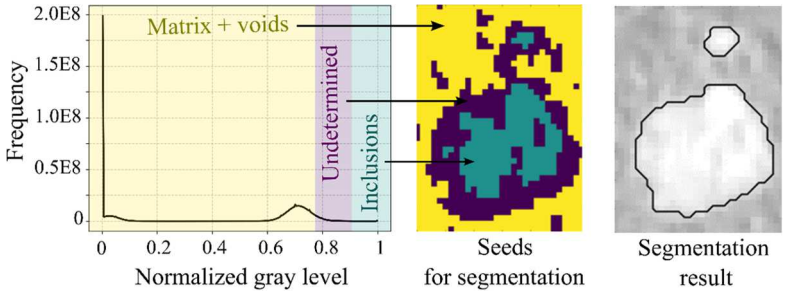

FIG. 10. — Inclusion (brighter than the matrix) segmentation from a µ-CT image: gray level histogram (left), seeds used to initialize the random walk algorithm (middle), segmentation result (black edges) overlaid on the denoised image (right).

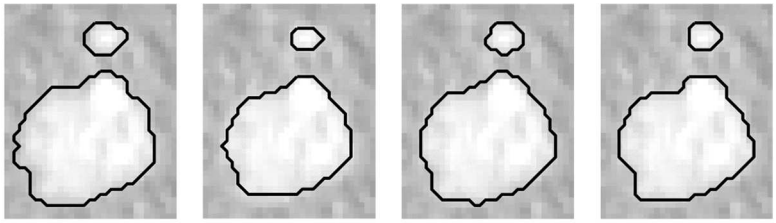

FIG. 11. — Segmentation of an inclusion on a µ-CT image using the random walk algorithm: sensitivity to the threshold values applied to determine the seeds for the inclusions and the matrix used for initialization of the algorithm.

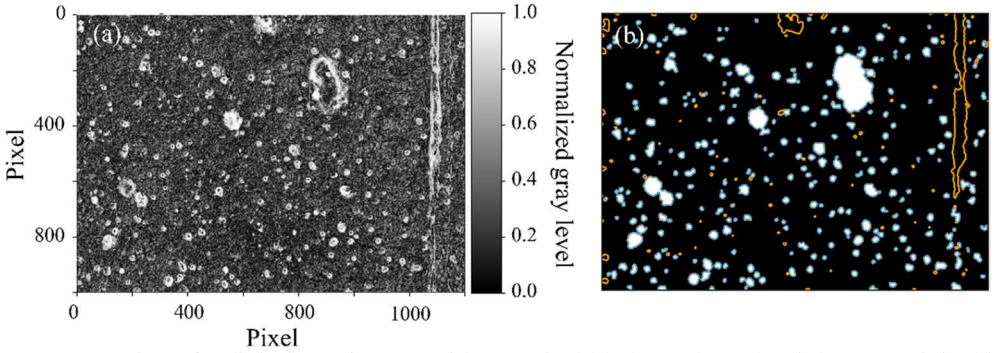

FIG. 12. — Segmentation of a digital OM image (with a vertical blade mark on the right): (a) original image; (b) result of segmentation with selection of the objects according to their size, shape and position (orange edges: deleted objects, blue edges: kept objects).

FIG. 13. — Separation by erosion and dilation of close inclusions detected on a digital OM image.

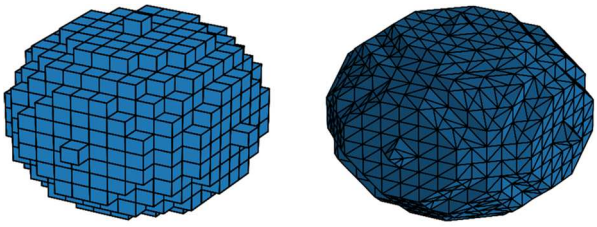

(a) (b)

FIG. 14. — Inclusion represented (a) by voxels and (b) by a triangular mesh obtained using the marching cubes algorithm.

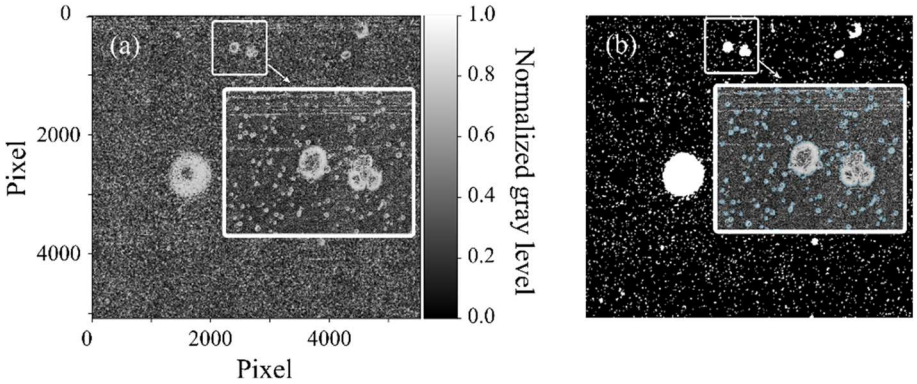

FIG. 15. — Analysis of a digital OM image obtained for the NR-N339 material: (a) raw image, (b) binarized image after segmentation and zoom showing the segmentation result (blue edges) overlaid on the original image.

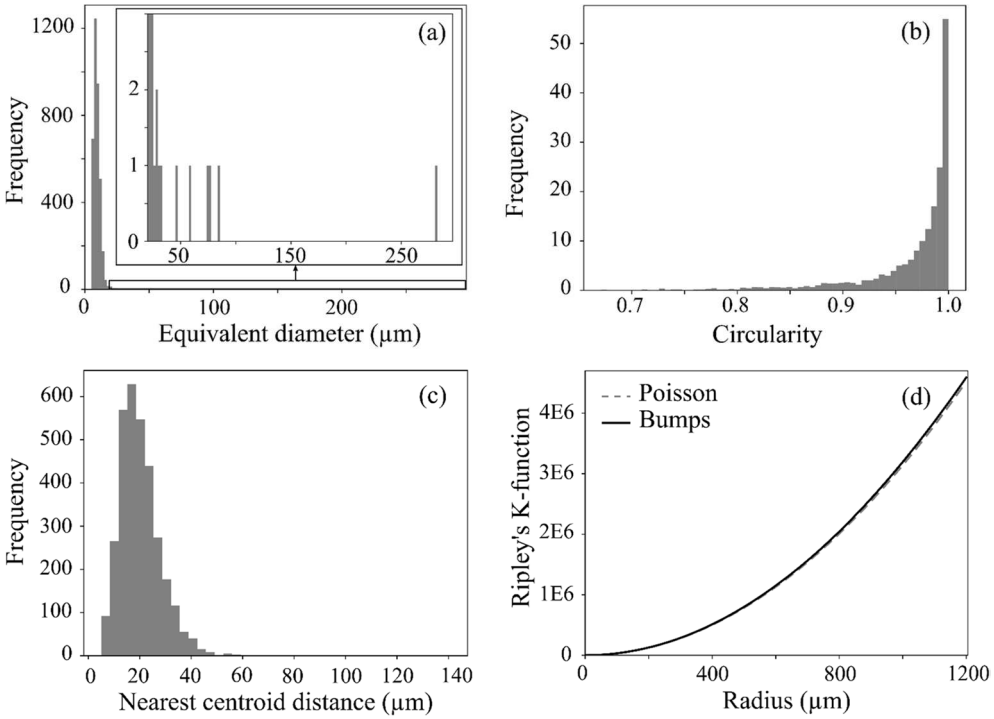

FIG. 16. — Characteristics of the 3237 bumps detected on the digital OM image shown in Fig. 15 obtained for the NR-N339 material: (a) histogram of the equivalent diameter of the circles having the same area as the bumps, (b) histogram of the circularity of the ellipses with the same area as the bumps, (c) shortest distance between the centroids of the bumps, (d) Ripley's K-function applied to the centroids of the bumps, compared to the one for a homogeneous Poisson point process (random point pattern).

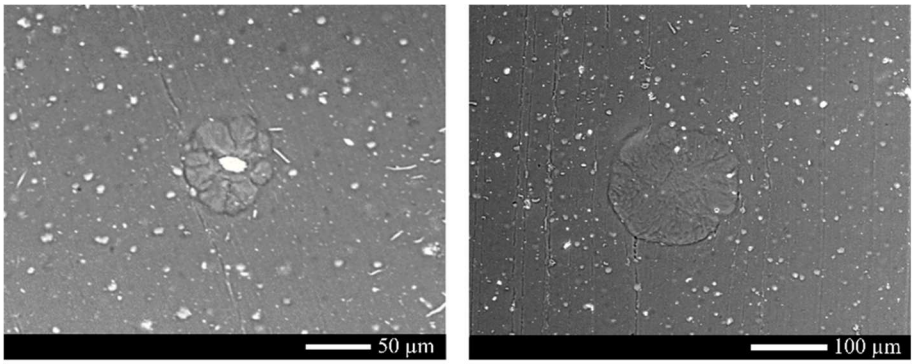

FIG. 17. — (a) Geode-type inclusion (only the envelope slightly darker than the matrix and the contour of the cavity brighter than the matrix are visible; the cavity is not) and (b) type 2 inclusion observed by SEM-BSE.

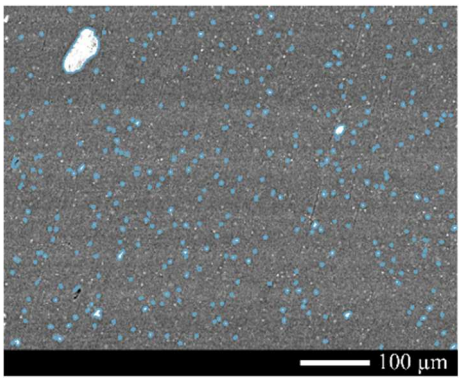

FIG. 18. — SEM-BSE image obtained for the NR-N339 material, with the segmentation result overlaid.

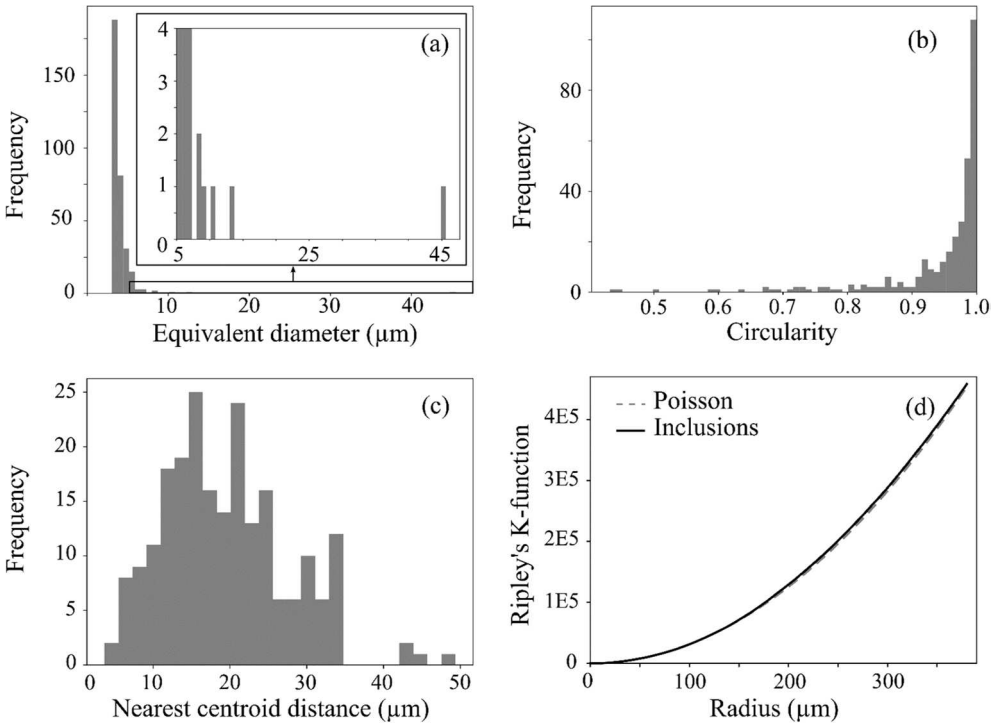

FIG. 19. — Characteristics of the 326 inclusions detected on the SEM-BSE image shown in Fig. 18 (b) obtained for the NR-N339 material: (a) histogram of the equivalent diameter of the circles having the same area as the inclusions, (b) histogram of the circularity of the ellipses with the same area as the inclusions, (c) shortest distance between the centroids of the inclusions with a size larger than 3.2 µm, (d) Ripley's K-function applied to the centroids of the inclusions, compared to the one for a homogeneous Poisson point process.

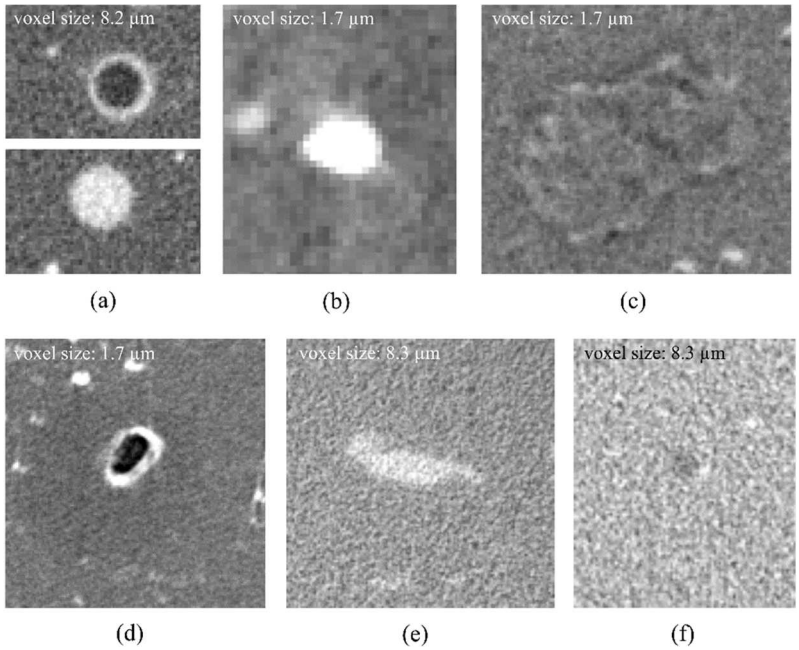

FIG. 20. — Inclusions observed by µ-CT: (a) glass beads (HGB on top, SGB on bottom), (b) metal oxide, (c) CB agglomerate, (d) geode-type, (e) type 1 and (f) type 2 inclusions.

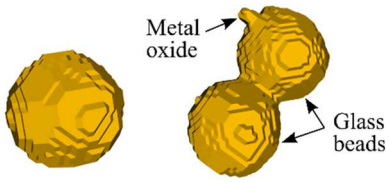

FIG. 21. — Examples of glass beads detected on the 8.3 µm resolution µ-CT images obtained for the NR-N339&SGB material: (a) glass beads well detected, (b) two glass beads and one metal oxide merged.

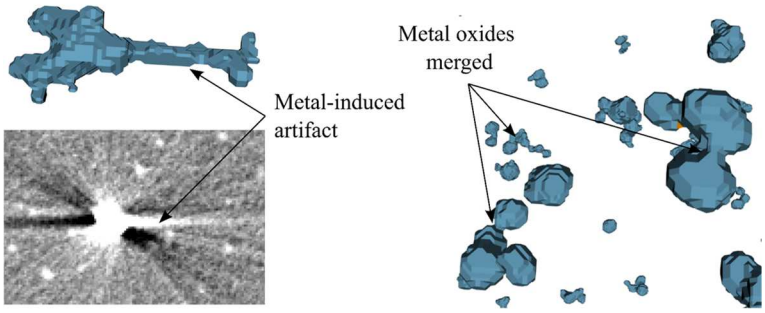

FIG. 22. — Metal-induced artifacts and metal oxides merged after segmentation of 8.3 µm resolution µ-CT images obtained on NR-N339 and IR-N339 materials.

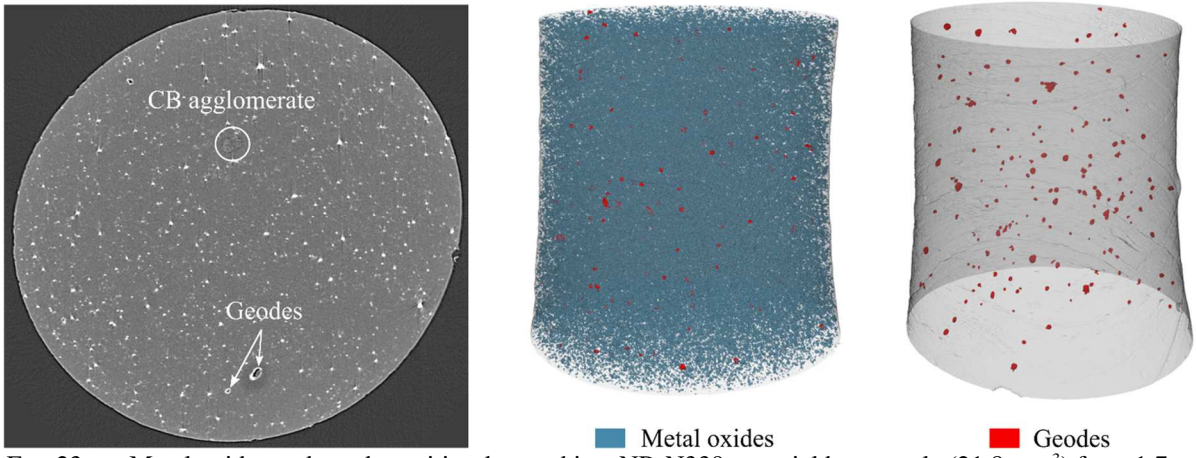

FIG. 23. — Metal oxides and geode cavities detected in a NR-N339 material bar sample (21.8 mm^3) from 1.7 µm resolution µ-CT.

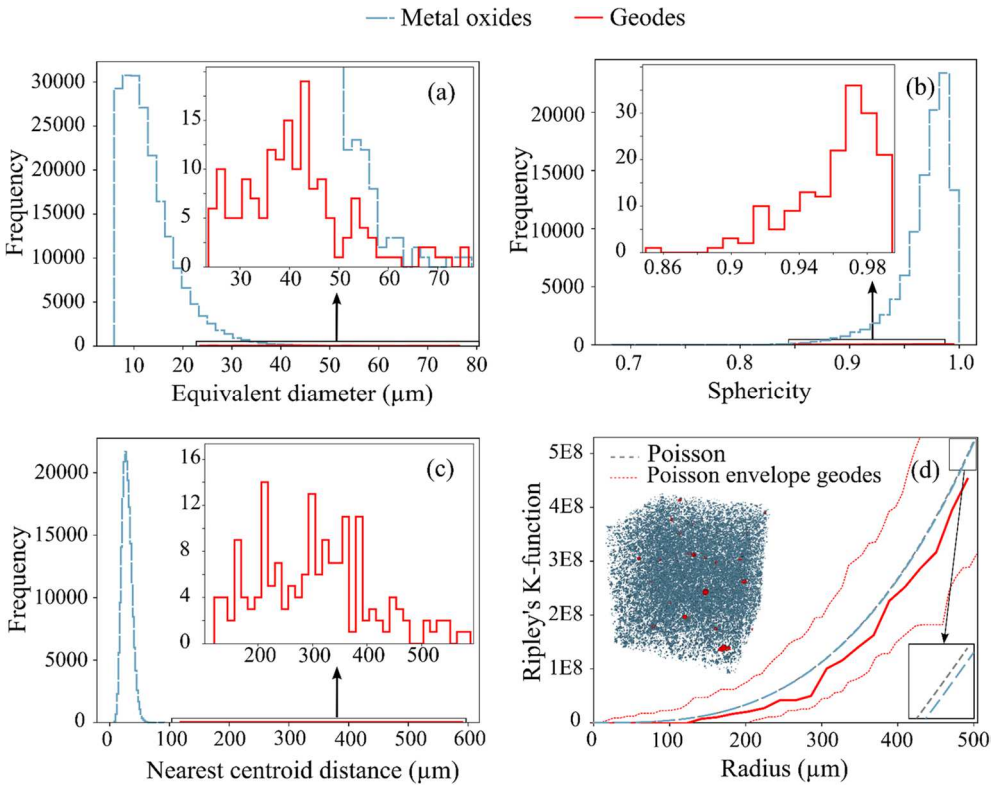

FIG. 24. — Characteristics of the 201109 metal oxides and the 165 geode cavities detected on the 1.7 µm resolution µ-CT shown in Fig. 23 obtained for the NR-N339 material: (a) histogram of the equivalent diameter of the spheres having the same volume as the inclusions, (b) histogram of the sphericity of the smallest ellipsoids encompassing the inclusions, (c) shortest distance between the centroids of the inclusions, (d) Ripley's K-function applied to the centroids of the inclusions, compared to the one for a homogeneous Poisson point process, for a 1656x1656x1656 μm^3 cube taken in the analyzed volume.

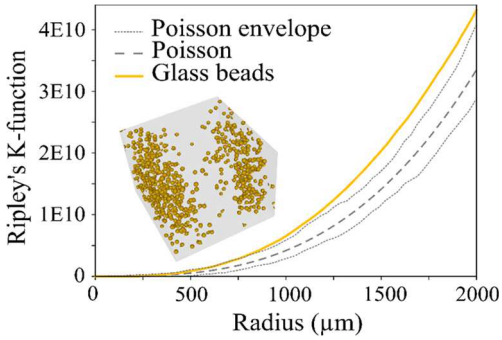

FIG. 25. — Glass beads detected on the 8.3 µm resolution µ-CT obtained for the NR-N339&SGB material: Ripley's K-function applied to the centroids of the inclusions, compared to the one for a homogeneous Poisson point process.

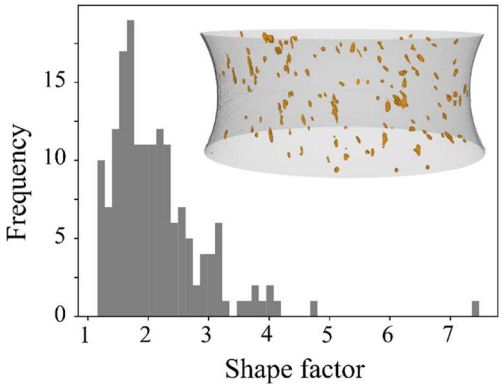

FIG. 26. — Histogram of the shape factor of type 1 inclusions detected on a 8.3 µm resolution µ-CT obtained for the NR/IR-N339 material (AE specimen).

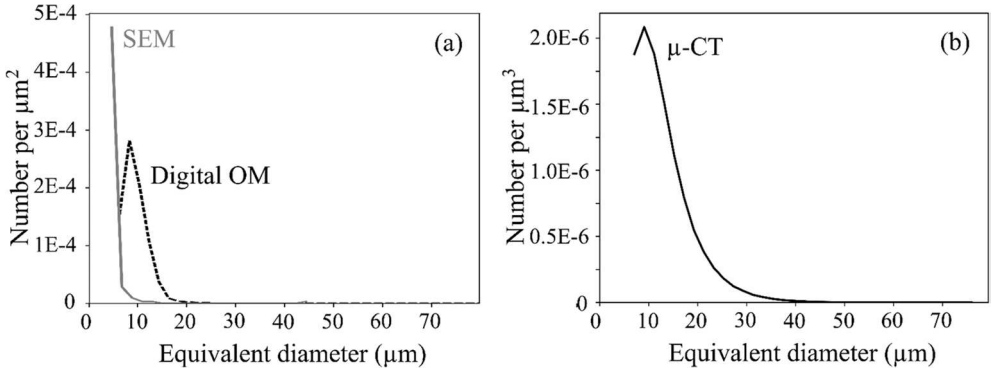

FIG. 27. — (a) Number of inclusions per unit area detected by digital OM and SEM-BSE and (b) number of inclusions per unit volume detected by µ-CT, versus the inclusion's equivalent diameter, for the NR-N339 material.

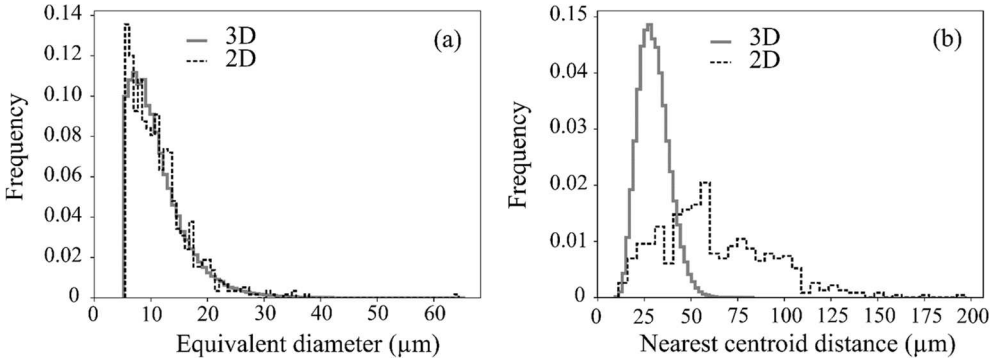

FIG. 28. — Comparison of the normalized histograms of (a) the equivalent diameter and (b) the shortest distance between the centroids of the inclusions (metal oxides and geodes) detected on a slice of the µ-CT (771 inclusions) and on the whole volume (201274 inclusions), for the NR-N339 material.

TABLES

TABLE 1

COMPARISON OF THE MOST COMMON TECHNIQUES USED IN THE LITERATURE TO STUDY THE DISPERSIONS OF INCLUSIONS (CB IN PARTICULAR) IN RUBBER MATERIALS IN RELATION TO THE SIX SPECIFICATIONS DEFINED IN THIS PAPER: + WHEN THE TECHNIQUE IS ABLE TO MEET THE SPECIFICATION, - WHEN IT IS NOT, +/- WHEN IT CAN MEET IT PARTIALLY.

Technique	1. Size of inclusions	2. Sensitivity, objectivity	3. Nature of inclusions	4. Quantitative description	5. Statistical description	6. Simplicity, robustness, efficiency
Transmitted light OM	+	+/-	-	+/-	+/-	+/-
DisperGRADER™	+	+/-	-	+/-	+/-	+
Dark field OM	+	+/-	-	+/-	+/-	+
Optical properties of CB	-	+/-	-	-	-	+/-
White light interferometry	+	+/-	-	+/-	+/-	+/-
TEM	-	+/-	+/-	+/-	-	-
SEM-SE	+	+/-	+/-	+/-	+/-	+/-
µ-CT	+	+	+/-	+	+	+/-
Roughness tester	+	+/-	-	-	+/-	+/-
AFM	-	+/-	-	+/-	-	+/-
Electrical resistivity	-	+	+/-	-	-	+

TABLE 2
COMPOSITION OF THE STUDIED MATERIALS IN PER HUNDRED OF RUBBER.

	NR-N339	NR/IR-N339	IR-N339	NR-N990	NR-N339&HGB	NR-N339&SGB
NR	100	75	-	100	100	100
IR	-	25	100	-	-	-
N339	29	29	29	-	29	29
N990	-	-	-	36	-	-
HGB	-	-	-	-	10	-
SGB	-	-	-	-	-	10
Processing agent	7	7	7	7	7	7
Anti-ozone wax	3.4	3.4	3.4	3.4	3.4	3.4
Antioxidant	3	3	3	3	3	3
Zinc oxide	4.1	4.1	4.1	4.1	4.1	4.1
Stearic acid	2	2	2	2	2	2
Sulfur	3.4	3.4	3.4	3.4	3.4	3.4
Accelerator	1	1	1	1	1	1

TABLE 3
PARAMETERS USED FOR μ-CT.

	AE2 specimens	Bar samples
Voltage	40 kV	40 kV
Power	10 W	4 W
Exposition time	30 s	20 s
Magnification	1	4
Source-object distance	60 mm	40 mm
Object-detector distance	35 mm	40 mm

TABLE 4

AREAS OBSERVED AND SPATIAL RESOLUTIONS OF THE IMAGES FOR THE THREE TECHNIQUES USED .

Technique	Digital OM	SEM	µ-CT	
			AE2 specimens	Bar samples
Area observed	7.7×7.7 mm^2	0.64×0.49 mm^2	$\pi 4.5^2 \times 6$ mm^3	$\pi 1.5^2 \times 2.9$ mm^3
Pixel or voxel size	0.385 µm	0.5 µm	8.3 µm	1.7 µm

TABLE 5
TYPES OF INCLUSIONS OBSERVED IN THE STUDIED MATERIALS: YES IF OBSERVED, NO IF NOT.

Material	Metal oxides	CB agglomerates	Geode-type	Type 1	Type 2	Glass beads
NR-N339	yes	yes	yes	no	no	no
NR/IR-N339	yes	yes	no	yes	yes	no
IR-N339	yes	yes	no	no	yes	no
NR-N990	yes	yes	no	no	no	no
NR-N339&HGB	yes	yes	no	no	no	yes
NR-N339&SGB	yes	yes	no	no	no	yes

TABLE 6

CHARACTERISTICS CONSIDERED TO DISTINGUISH THE INCLUSION TYPES FROM EACH OTHER ON μ-CT IMAGES.

Inclusion type	Characteristics
Metal oxides	Solid, bright, size < type 1 and glass beads; no size limit if no type 1 and glass beads
CB agglomerates	Absence of metal oxides in the area, few dark voxels (porosities?)
Geode-type	Bright cavity border, size > 27 voxels (resolution 1.7 μm)
Type 1	Solid, bright, equivalent diameter > 100 μm
Type 2	Solid, dark, equivalent diameter > 60 μm, sphericity > 0.7
Glass beads	Bright, equivalent diameter > 150 μm

TABLE 7

CHARACTERISTICS OF THE (A) GLASS BEADS, (B) METAL OXIDES, (C) CB AGGLOMERATES LARGER THAN 40 µM, (D) CAVITY OF THE GEODE-TYPE INCLUSIONS, (E) TYPE 1 INCLUSIONS AND (F) TYPE 2 INCLUSIONS, IN THE STUDIED MATERIALS, DETERMINED FROM µ-CT PERFORMED ON BAR SPECIMENS WITH A RESOLUTION OF 1.7 µM AND/OR ON AE2 SPECIMENS WITH A RESOLUTION OF 8.3 µM: VOLUME ANALYZED, NUMBER, VOLUME FRACTION, EQUIVALENT DIAMETER AND SPHERICITY OF THE INCLUSIONS DETECTED AND DISTANCE TO THE NEAREST NEIGHBOR CENTROID.

Material	Specimen type / vol. (mm^3)	Number	Volume fraction (%)	Equivalent diameter (µm) min/mean±std/max	Sphericity (-) min/mean±std/max	Shortest distance (µm) min/mean±std /max
(a) Glass beads						
NR-N339&HGB	AE2 / 286	1989	3.6	152/212±26/397	0.40/0.82±0.10/0.92	204/334±80/758
NR-N339&SGB	AE2 / 285	1260	2.2	151/209±21/333	0.49/0.85±0.07/0.92	212/364±110/965
(b) Metal oxides						
NR-N339	AE2 / 252	40717	0.94	31/45±12/315	0.45/0.88±0.05/0.94	41/110±32/343
	bar / 22	201109	1.9	6/13±6/77	0.23/0.85±0.06/0.94	8/29±8/91
NR/IR-N339	AE2 / 235	6394	0.18	31/46±14/100	0.55/0.87±0.04/0.93	45/190±71/623
	bar / 16	132392	1.1	6/12±5/96	0.40/0.84±0.05/0.93	9/34±10/88
IR-N339	AE2 / 253	60658	1.67	31/47±20/237	0.45/0.87±0.06/0.95	25/100±26/242
	bar / 18	293811	3.1	6/12±6/116	0.22/0.85±0.07/0.93	9/28±7/77
NR-N990	bar / 17	115233	1.4	6/13±12/137	0.42/0.87±0.06/0.95	9/31±9/88
NR-N339&HGB	AE2 / 286	28619	0.65	30/46±13/150	0.54/0.89±0.04/0.95	43/125±39/356
NR-N339&SGB	AE2 / 285	26356	0.51	30/44±12/149	0.56/0.89±0.04/0.95	40/129±41/370
(c) CB agglomerates larger than 40 µm						
NR-N339	bar / 22	15	0.016	47/65±26/155	-	-
NR/IR-N339	bar / 16	3	0.002	51/56±4/61	-	-
IR-N339	bar / 18	9	0.05	54/88±56/238	-	-
NR-N990	bar / 22	7	0.002	40/47±8/60	-	-
(d) Cavity of the geode-type inclusions						
NR-N339	bar / 22	165	0.03	24/41±11/76	0.40/0.74±0.11/0.90	119/301±104/590
(e) Type 1 inclusions						
NR/IR-N339	AE2 / 235	166	0.10	100/129±32/288	0.53/0.74±0.07/0.87	163/1363±251/1363
	bar / 16	1	0.03	216/216±0/216	0.51/0.51±0/0.51	-
(f) Type 2 inclusions						
NR/IR-N339	AE2 / 235	120	0.02	60/90±16/120	0.70/0.78±0.03/0.84	123/708±277/1504

TABLE 8

EVALUATION OF THE APPLICABILITY OF THE TECHNIQUES USED, ASSOCIATED WITH THE IMAGE PROCESSING DEVELOPED, TO CHARACTERIZE THE INCLUSIONS IN RELATION TO THE SIX SPECIFICATIONS DEFINED IN THIS PAPER: + WHEN THE TECHNIQUE IS ABLE TO MEET THE SPECIFICATION, - WHEN IT IS NOT, +/- WHEN IT CAN MEET IT PARTIALLY.

Technique	1. Size of inclusions	2. Sensitivity, objectivity	3. Nature of inclusions	4. Quantitative description	5. Statistical description	6. Simplicity, robustness, efficiency
Digital OM with the image processing developed	+	+/-	-	+/-	+/-	+/-
SEM-BSE with the image processing developed	+	+/-	+-	+	+/-	+/-
µ-CT with the image processing developed	+	+	+	+	+	+/-

TABLE 9

ABILITY OF THE TECHNIQUES USED TO OBSERVE, DETECT AND DISTINGUISHED THE INCLUSIONS FROM THE MATRIX AND FROM EACH OTHER: O IF VISUALLY OBSERVABLE, D IF DETECTABLE BY IMAGE PROCESSING (OR MANUALLY OR VISUALLY), X IF NATURE CANNOT BE IDENTIFIED.

	Digital OM	SEM-BSE	µ-CT
Metal oxides	x	O & D	O & D
CB agglomerates	x	x	O & manual D (resolution 1.7 µm, size > 40 µm)
Geode-type	x	O & ≈D (cavity)	O & ≈D (resolution 1.7 µm, cavity)
Type 1	x	x	O & D
Type 2	x	O	O & D (resolution 8.3 µm)
Glass beads	O & visual D	O & D	O & D